We would like to thank the reviewers for spending time on this paper and for providing an interesting set of comments. The comments have helped the authors and have improved the paper. Please find a point-by-point discussion and answer of the issues raised by the reviewers. To facilitate the work of reviewers and the editor, the reviewer's comments and suggestions are preceding each reply in italic face.

The corrections are highlighted in yellow in the article (after the author comments).

Reviewer 1

All the corrections given by the reviewer have been done in the text.

1) Please use "rawinsoundings" and rawinsondes" where appropriate.

Yes, the correction has been done.

2) *Preferably referred as "S", as most commonly used in the lidar literature.*

Yes, but for us, S is also the lidar signal. So, we prefer to use LR for lidar ratio.

3) *not appropriate citations. Please use more recent and well established ones (e.g see in the ICCP 2014)*

The references have been changed and the IPCC has been cited.

4) *Please use more recent and well established ones (e.g see in the ICCP 2014)*

The reference to ICCP (2014) has been added. Nevertheless, even if new references explain the role of aerosol, this is not new in atmospheric science. Thus, the earlier references have to be cited.

5) *This is not true. It has to be very clearly presented (e.g., put in ( ) which instruments are available with what range and time resolution).*

We agree that this sentence is awkward. It was withdrawn.

6) *This part is too "bavardeux". It has to be completely revised. Please cite more updated literature.*

We do not agree, it is not "bavardeux". It is a fast overview of the lidar use for atmospheric moisture survey. As asked by the reviewer in its next remark, we have added a reference to the DWD Ramses lidar.

7) *Of course this kind of instrumentation exists since the 90s'. and many relevant instruments have been developed so far, some of them on an operational level (cite here the existing instruments such as the DWD Ramses lidar, the ARM lidar etc.).*

The ARM lidar has been cited in the previous section. This is the reason of this introductive part. Yes, the DWD has to be cited and we have added this quote.

8) *cite here according to which standards*

The standard has been added (EN 60825-1).

9) *not clearly written. pease rephrase*

We have added complementary information as also asked by the third reviewer:
“The receiver is composed of 3 distinct detection boards using small collector diameters of 15 cm. The total number of detection channels is four. Note that the reason to have separate paths for the two Raman channels is to be able to set-up independently each channel to keep as much flexibility as possible. Hence, we can easily replace a detection board to change the lidar measurements.”

10) *please correct inside all manuscript*

We have replaced “interferential filter” by ‘interference filter” in all manuscript.

11) *insert "(FWHM)"*

It has been added.

12) *Please provide citations here!*

The reference to Bock et al. (2009) has been added.

13) *Start a new paragraph here!*

The correction has been made.

14) *not clear! please rephrase*

We have replace “lower” by “smaller”.

15) *insert "measurement"*

The correction has been done.

16) *have already been*

The correction has been done.

17) *insert "presenting"*

The correction has been done: “After presenting the lidar calibration and the assessment of the different error sources, we will present a study on a typical meteorological situation using a synergy between the WVMR and aerosols lidar measurements.”.

18) *This statement is false and has to be replaced, as there are a lot of data in the literature. There are several papers for lidar ratio at 355 nm (Mona et al., 2012; SAMUM papers;*

doi:10.1029/2007JD009028; doi:10.1029/2005JD006190; doi:10.1029/2004GL019881; and many others)

We agree, the end of the sentence has been removed. The reference to Mona et al. (2012) and Balis et al. (2004) have been added.

19) *I do not like this text at all. Please rephrase it completely, referring to the current state of the art of the UV Raman lidar technique. No need to go back to the early lidar papers (of the year 1962)*

This section has been entirely rephrased to highlight the specificity of our system compared to the current state of the art.

20) *Corrections on Fig. 1*

The correction has been made *(P-pol => p-pol, S-pol => s-pol).*

<u>Reviewer 3</u>

1) *L43: I think that the references of Melfi et al.(1989) and Kulmala et al. (1993) are not suitable because they did not directly study the influence of water vapor to the energy balance of the atmosphere. Please cite more suitable papers.*

The references have been changed and the IPCC has been cited.

2) *L79: I don't understand what the "natural" evolution of the lidar is. Please explain it.*

"Natural" is not to consider alone, it is a natural evolution in the frame of scientific programs HyMeX and ChArMEx, as explained in the text. We have removed "natural".

3) *L102: Is the word "than" grammatically correct?*

We have corrected the sentence by; "The WALI instrument has been developed at LSCE based on the same technology **as** its precursor instruments LESAA".

4) *L115: Do you use 3 receiving telescope? Please make clear the explanation (also Fig. 2).*

Yes, we use 3 receiving telescopes. In fact, the explanation is given later. We have move the sentence and complete it: "The receiver is composed of 3 distinct detection boards using small collector diameters of 15 cm. The total number of detection channels is four. Note that the reason to have separate paths for the two Raman channels is to be able to set-up independently each channel to keep as much flexibility as possible. Hence, we can easily replace a detection board to change the lidar measurements."

5) *L119: compactedness ! compactness*

The correction was made.

6) L127: Do you mean that you use the separate HV supply unit for the Raman nitrogen and water vapor channels? Please correct the sentence.

The sentence has been corrected: "As separate HV supply units for the Raman nitrogen and water vapor channels are used, a careful calibration of the relative channel gain versus HV has to be performed."

7) L145: The word "other' might be necessary before "than" (please check grammar).

The correction has been done.

8) L163: Add the explanation of the lidar ratio (i.e. particle extinction-to-backscatter ratio).

The explanation has been added.

9) L170: What value of A you used in the study?

We have considered a value of 1 for the error budget. The value has been given in the section 4.

10) L175: "total" should be "unity".

"total" has been replaced by "complete" as asked by the first reviewer.

11) L195: Which altitude is correct of full overlap, 500 m, 700 m (L175) or 200-300 m (L120 and Table 1)?

As explained, the correct value is 200-300 m, but for the water vapor channel the field diaphragm did not collect the entire image field in the optical configuration used. This leads to a degraded overlap factor.

*12) L198: How do you correct the spectral dependency of the aerosol extinction be-*tween the two Raman wavelengths?

It is not a major error as explained in the text and the correction is done with an Angstrom exponent of 1 (see section 4). The aerosol channels of the lidar give the vertical profile of the aerosol extinction coefficient.

21) L204: What is the reference altitude you used in this study?

The altitude range has been given in the text: "For this study, z_0 has been chosen above the aerosol layers, between 4 and 6 km amsl."

22) L208: What value is used for beta_E(z0) in Eq. (6).

As explained in section 2.2, the molecular extinction and backscatter coefficients are determined with the polynomial approximation proposed by Nicolet (1984). The value is a function of the altitude.

23) Is the word "raowindsounding" well accepted in the community of the atmospheric science? Please check it.

We have made the correction by "rawinsounding".

24) L259: Please explain the method for determinng the overlap factor ratio.

A complementary explanation has been given in section 3: "*K* is first assessed using the upper part of the rawinsounding profile and ξ is then retrieved from the lower part (below 0.8 km amsl)."

17) L262: What height range or point did you compare the water vapor mixing ratio between the lidar and radiosonde to obtain the calibration constant and how did you compare the ratios (e.g. least square method)? Please explain.

We have added the method: "The calibration adjustments have been computed using the minimum of the mean square deviation between the lidar and the rawinsounding profiles."

18) L344: Please give a comment on the uncertainty of the overlap function and its influence on the derived water vapor mixing ratio.

The discussion about the effect of the overlap function on the WVMR relative error is given in section 4 (Calibration). It leads to a relative uncertainty ~ 4% for altitudes between 0.3 and 0.80 km amsl.

19) L439:"southwest" ! "southwesterly"?

The correction has been made.

20) L462: "stronger" should be "higher". Please correct the same word in L476 and L480.

The corrections have been made.

21) L470. Please explain how the dust plumes destabilized the air masses in more detail.

Dust aerosol presence in the atmospheric column impacts the radiative balance and by this way modifies the vertical equilibrium by increasing the convection. This point has been added in the text.

22) L518: The paper of Smullin and Fiocco (1962) is not cited in the reference list.

We do not cite this paper anymore in our revised manuscript.

23) Fig. 3: The photograph of the lidar-van is not clear. It would be better if it is replaced with the close-up of the van.

The picture has been resized for better clarity.

25) Fig. 8 The "S355" in the legend should be "PR355".

The corrections have been done on Figures 4 and 7, and a sentence has been modified in the text: "The presence of clouds, highlighted on the elastic range-corrected lidar signal S355, prevents us from verifying the agreement between the instruments over 1.6 km amsl."

25) Caption of Fig. 12: Add the explanation of a)-f). Are they corresponds to the time periods of Table 2?

The dates and time are given in the caption of Fig. 12 for each case. We have added the reference to Table 2: "The time periods from a) to f) correspond to the ones of Table 2".

The mobile Water vapor Aerosol Raman LIdar and its implication in the frame of the HyMeX and ChArMEx programs: application to a dust transport process

Patrick Chazette, Fabien Marnas, and Julien Totems

Laboratoire des Sciences du Climat et de l'Environnement (LSCE), UMR8212, Laboratoire mixte CEA-CNRS-UVSQ, CEA Saclay, 91191 Gif-sur-Yvette, France.

Abstract.

The increasing importance of the coupling of water and aerosol cycles in environmental applications requires observation tools which allow simultaneous measurements of these two fundamental processes for climatological and meteorological studies. In this purpose, a new mobile Raman lidar, WALI (Water vapor and Aerosol LIDAR), has been developed and implemented within the framework of the international HyMeX/IODA-MED and ChArMEx programs. This paper presents the key properties of this new device and its first applications to scientific studies. The lidar uses an eye-safe emission in the ultra-violet range at 354.7 nm and a set of compact refractive receptors. Cross-comparisons between rawinsoundings performed from balloon or aircraft and lidar measurements have shown a good agreement in the derived water vapor mixing ratio (WVMR). The discrepancies are generally less than 0.5 g/kg and therefore within the error bars of the instruments. A detailed study of the uncertainties was conducted and shows a 7 to 11% accuracy of the WVMR retrieval, which is largely constrained by the quality of the calibration. It also proves that the lidar is able to measure the WVMR during daytime over a range of about 1 km. The WALI system otherwise provides measurements of aerosol optical properties such as the lidar ratio (LR) or the

particulate depolarization ratio (PDR). An important example of scientific application addressing the main objectives of the HyMeX and ChArMEx programs is then presented, following an event of desert dust aerosols over the Balearic Islands. This dust intrusion may have had a significant impact on the intense precipitations that occurred over southwestern France and the Spanish Mediterranean coasts. During this event, the LR and PDR values obtained are in the ranges of ~45-63±6 sr and 0.1-0.19±0.01, respectively, which is representative of dust aerosols. The dust layers are also shown to be associated with significant WVMR, i.e between 4 and 6.7 g/kg.

1 Introduction

By the end of the 21st century, climate models forecast a significant increase in the loss of fresh water in densely populated areas. For instance, the decrease of fresh water reserves around the Mediterranean Sea has been assessed to be 40 % higher for 2070-2090 than for 1950-1999 (*Sanchez-Gomez et al.*, 2009). These results should be evaluated in the context of rising anthropogenic pressure in the Mediterranean region, with a population growth expected in the range of 300% around the Mediterranean basin within the next 25 years (with more than 500 million inhabitants). The Mediterranean area has thus been identified as a hot-spot in the projections of future climate change (*Giorgi and Lionello*, 2008) where the water-vapor mixing ratio is a key meteorological parameter for the energy balance of the atmosphere (e.g. Held and Soden, 2000; IPCC, 2013).

Moreover, it is now known that the cycles of aerosols, clouds and water-vapor are closely coupled within the climate change scenarios. Indeed, water-vapor is involved in the aerosol and cloud formation when aerosols contain hygroscopic components (e.g. *Larson and Taylor*, 1983; *Rood et al.*, 1987; *Radriamiarisoa et al.*, 2006) and thus influences the Earth-Atmosphere radiative balance. Aerosol hydration remains one of the largest sources of uncertainty in the climate models (*Covert et al.*, 1979; *Boucher and Anderson*, 1995; *Haywood et al.*, 1997; IPCC, 2014). Aerosols also lead to a visibility reduction in the atmosphere, which impacts the socio-economical activities. As the densely populated areas of the planet are especially characterized by their vulnerability to changes in the coupled cycles of water and aerosol, precise measurements are now necessary to assess the model uncertainties in both the water-vapor mixing ratio and the aerosol amounts in the lower and middle troposphere.

As written by *Whiteman et al.* (1992), lidar is a well-established technique for measuring the water-vapor mixing ratio in the atmosphere. *Cooney* (1970) and *Melfi et al.* (1969) showed as early as the late 1960's that the Raman lidar is a powerful tool for this measurement and *Vaughan et al.* (1988) used for the first time Raman lidar to perform water-vapor mixing ratio measurements up to the tropopause. Following these pioneer works, *Ansmann et al.* (1992) performed simultaneously measurement of the water-vapor mixing ratio and aerosol optical properties, *Turner et al.* (1999) used Raman lidar in continuous measurements in the framework of the atmospheric radiation measurement program (ARM), and *Veselovskii et al.* (2000) also yielded profiles of the water-vapor mixing ratio in the troposphere. More recently, the German Meteorological Service has been equipped with a Raman lidar (*Reichardt et al.*, 2012). The differential absorption lidar technique (e.g. *Noah et al.*, 1994; *Bruneau et al.*, 2001) could also be used but requires greater instrumental constraints and makes it difficult to comply with eye-safety conditions. Lidar is also an often-used instrument for aerosol survey (*Fiocco and Grams*, 1964) and particularly Raman lidar (e.g. *Melfi et al.*, 1989; *Ansmann et al.*, 1992; *Turner et al.*, 1999). More recently, an eye-safe, compact and light Nitrogen-Raman lidar has been developed at the Laboratoire des Sciences du Climat et de l'Environnement (LSCE) to track the aerosol pollution around Paris as well as the ash emitted in the atmosphere by the Eyjafjallajökull volcano (*Royer et al.*, 2010; *Chazette et al.*, 2011). The evolution of such a lidar, in the frame of the scientific programs Hydrological cycle in the Mediterranean eXperiment (HyMeX, http://www.hymex.org/) and Chemistry-Aerosol Mediterranean Experiment (ChArMEx, http://www.mistrals-home.org), was the addition of a water-vapor Raman channel.

We present in this paper the new transportable eye-safe and mobile Water-vapor and Aerosol Raman LIdar (WALI) that is able to measure simultaneously the water-vapor mixing ratio (WVMR) and the aerosol optical properties with a sufficient reliability for meteorological and climatological studies in the lower and middle troposphere. The first results obtained on the retrieval of the WVMR and aerosol optical properties will be presented and discussed hereafter following the fall campaign of the HyMeX/IODA-MED (Innovative Observing and Data Assimilation systems for the MEDiterranean Weather) program. The datasets gathered on aerosol properties also represents the first measurements provided to the ChArMEx program.

In a first section, the Raman lidar will be presented along with the experimental set-up. The classical theoretical approaches for the retrieval of the WVMR and aerosol optical properties will be also reminded. For the lidar calibration, a comparison to WVMR vertical soundings performed by rawinsoundings and aircraft measurements will be presented in a second section. The main uncertainties will be assessed and discussed in a third section. In a fourth section we will analyze an example of dust event observed in the frame of the HyMeX/IODA-MED and ChArMEx programs. Finally, the conclusions will recall the main characteristics of the instrument and the first results obtained.

2 Experimental and theoretical tools

The WALI instrument is here described as well as the signal processing used for the retrieval of both the WVMR and the aerosol optical properties. The experimental sites where lidar measurements have been performed are also presented.

2.1 Technical characteristics of WALI

The WALI instrument has been developed at LSCE based on the same technology as its precursor instruments LESAA (Lidar pour l'Etude et le Suivi de l'Aérosol Atmosphérique, (*Chazette et al.*, 2005) and LAUVA (Lidar Aérosol UltraViolet Aéroporté (*Chazette et al.*, 2007; *Raut and Chazette*, 2009). It is a home-made instrument mainly dedicated to atmospheric research activities.

The lidar operates with an emitted wavelength of 354.7 nm and is designed to fulfill eye-safety standards (EN 60825-1). Its emitter is a pulsed Nd:YAG laser (BRILLANT) manufactured by the QUANTEL company (www.quantel.com). The acquisition system is based on a PXI (PCI eXtensions for Instrumentation) technology with 12 bits digitizers at 200 MS/s (Mega sampling by second) manufactured by the National Instruments company. Its main characteristics are summarized in Table 1. During all the experiment the acquisition was performed for mean profiles of 1000 laser shots leading to a temporal sampling close to 1 minute. The UV pulse energy is ~60 mJ and the pulse repetition frequency is 20 Hz.

A schematic representation of WALI is given in Figure 1. The receiver is composed of 3 distinct detection boards using small collector diameters of 15 cm. The total number of detection channels is four. Note that the reason to have separate paths for the two Raman channels is to be able to set-up independently each channel to keep as much flexibility as possible. Hence, we can easily replace a detection board to change the lidar measurements.

Using short focal length refractive telescopes instead of a reflector ensures a low altitude overlap for the lidar and increases its stability, transmittance and compactness. The wide field-of-view (FOV) ~2.3 mrad allows a full-overlap of the transmission and reception paths beyond ~ 200-300 m. On each channel, optical detection is performed by a photomultiplier tube placed behind an interference filter and a focusing lens. The amplification gain of the tube between its anode and cathode is directly linked to the input high voltage (HV) chosen by the lidar acquisition software. HV variation allows optimizing the detection dynamic for both nighttime and daytime measurements (with strong sky background light). As separate HV supply units for the Raman nitrogen and water vapor channels are used, a careful calibration of the relative channel gain versus HV has to be performed.

The first board is dedicated to the detection of the elastic molecular, aerosols and cloud backscatter from the atmosphere. Two different channels are implemented on that board to detect i) the total (co-polarized and cross polarized with respect to the laser emission) and ii) the cross-polarized backscatter coefficients of the atmosphere. The separation between the two beams is carried out using a beam-splitter and a Brewster plate. The interference filters (IF1), with spectral bandwidths of 0.2 nm (FWHM), are manufactured by Barr Associates. This reception channel design is similar to the one used for previous studies on tropospheric aerosols (e.g. *Royer et al.*, 2011; *Chazette et al.*, 2012). The second and third boards are dedicated to the measurements of the inelastic nitrogen (N_2-channel) and water vapor (H_2O-channel) Raman backscattered signals. They measure the backscattered Stokes component of the inelastic vibrational Raman scattering because this process is much more likely at the typical tropospheric temperatures (compared to the anti-Stokes component of Raman scattering). Such scattering happens at a larger wavelength than that emitted, i.e. ~386.6 nm and ~407.5 nm for N_2- and H_2O-channel, respectively. The measured water-vapor Raman signal is ~4 orders of magnitude (~3 orders for the nitrogen Raman signal) less than the elastic backscattered signal. Therefore, the H_2O-channel was found to require an extremely high rejection of all radiation apart from the Raman Stokes central peak, with a transmission ratio approaching 10 orders of magnitude, assuming a complete rejection of the elastic Rayleigh-Mie return (*Whiteman et al.*, 1992; *Whiteman et al.*, 2007). This is done by using a dichroic plate, as drawn in Figure 1, associated to a specific interference filter. The spectral bandwidth of this interference filter (IF3), also built by Barr Associates, is 0.3 nm to optimize the contribution of the rotational lines considering the signal to noise ratio. The N_2-channel is equipped with both a Brewster plate to decrease the background sky contribution and a Barr Associate interference filter (IF2) with a 0.2 nm spectral bandwidth. Note that, considering the spectral bandwidths of the interference filters used here, the Raman backscatter cross sections do not depend on the atmospheric temperature (*Bribes et al.*, 1976; *Penney and Lapp*, 1976; *Whiteman et al.*, 1992).

2.2 Lidar signal parameterization

The range corrected lidar signals S_λ at wavelength λ of a ground-based lidar situated at the altitude z_G above the mean sea level (amsl) is given as a function of backscatter coefficient β_j, and aerosol (molecular) extinction coefficient $\alpha_{a(m)}$ against altitude z by (e.g. *Measures*, 1984)

$$S_\lambda(z) = C_\lambda \cdot F_\lambda(z) \cdot \beta_\lambda(z) \cdot$$

$$exp\left(-\int_{z_G}^{z}\left[(1+\eta_{m\lambda}) \cdot \alpha_m(z') + \left(1+\eta_{a\lambda}(z)\right) \cdot \alpha_a(z')\right] \cdot dz'\right) \quad (1)$$

Where: i) for the elastic channel at $\lambda =$ 354.67 nm (subscript E thereafter), $\beta_E(z) = k_f \frac{3\alpha_m(z)}{8\pi} + \frac{\alpha_a(z)}{LR(z)}$, is the sum of the molecular (m, $\beta_m(z) = k_f \frac{3\alpha_m(z)}{8\pi}$) and the aerosol (a, $\beta_a(z) = \frac{\alpha_a(z)}{LR(z)}$), with k_f the King factor of air (King, 1923) and LR the lidar ratio (particle extinction-to-backscatter ratio), ii) for the nitrogen Raman channel at $\lambda =$ 386.63 nm (subscript N thereafter), $\beta_N(z) = N_N(z) \cdot \sigma_N^\pi$, with the nitrogen density profile N_N(z), and iii) for the water-vapor Raman channel at λ = 407.5 nm (subscript H thereafter), $\beta_H(z) = N_H(z) \cdot \sigma_H^\pi$, with the water vapor density profile N_H(z). σ_x^π stands for the Raman differential backscatter cross section of the nitrogen (x = N) or water-vapor (x = H) channels. Coefficients $\eta_{m\lambda} = \left(\frac{\lambda}{354.67}\right)^{-4.09}$ and $\eta_{a\lambda}(z) = \left(\frac{\lambda}{354.67}\right)^{-A(z)}$ are used to take into account the spectral dependency effects due to the molecules and aerosols (via the Angstrom exponent A), respectively. Note that only zenithal lidar measurements have been performed during this work. C_λ are the instrumental constants. F_λ are the overlap functions, which have been experimentally measured during the campaign for each channel and shown on Figure 2. The overlap function of the H_2O-channel has been deduced from both that of the N_2-channel and the calibration in terms of WVMR hereafter presented. It is not complete under ~0.7 km because the field diaphragm did not collect the entire image field in the optical configuration used. Hence, a correction, which is included in the calibration process, has to be applied.

The molecular extinction and backscatter coefficients are determined with the polynomial approximation proposed by *Nicolet* (1984) using a reference atmospheric density calculated from ancillary measurements (e.g. *Chazette et al.*, 2012). The uncertainty on the a priori knowledge of the molecular contribution has been previously assessed to be lower than 2% (*Chazette et al.*, 2010). Considering $k_f = 1$ leads to an overestimation on the molecular volume backscatter coefficient of only 1.5% at 355 nm (*Collis and Russel*, 1976).

2.2.1 Water-vapor mixing ratio

The WVMR (r_H) is defined as the mass of water vapor divided by the mass of dry air in the same volume:

$$r_H(z) = \frac{N_H(z)}{N_N(z)} \cdot \frac{M_H}{M_N} \cdot r_N \qquad (2)$$

where r_N is the nitrogen mixing ratio that can be considered as a constant in the troposphere. M_H and M_N are the molar masses of water-vapor and nitrogen, respectively. The WVMR can be directly derived from the ratio of the H_2O-channel and N_2-channel as

$$r_H(z) = K \cdot \xi(z) \cdot \frac{S_H(z)}{S_N(z)} \cdot exp\left(-[\eta_{mN} - \eta_{mH}] \cdot \int_{z_G}^{z} \alpha_m(z') \cdot dz' - \int_{z_G}^{z} [\eta_{aN}(z') - \eta_{aH}(z')] \cdot \alpha_a(z') \cdot dz'\right) \quad (3)$$

where K is the instrumental constant, expressed as

$$K = \frac{C_N}{C_H} \cdot \frac{\sigma_N^{\pi}}{\sigma_H^{\pi}} \cdot \frac{M_H}{M_N} \cdot r_N \quad (4)$$

ξ is the ratio between the overlap factors of the N_2-Raman and H_2O-Raman channels gradually approaching unity with altitude and reaching it around 700 m. Both K and ξ have to be assessed during a calibration procedure. In the second part of the equation, the second term represents the atmospheric corrections associated to the spectral dependencies of the extinction properties of both molecules and aerosols.

2.2.2 Aerosol optical properties

The retrieval of the aerosol optical properties coupled to backtrajectory analyses can contribute to the identification of the air mass origin and to the radiative balance studies above the Mediterranean basin. Those properties are obtained using the following procedure. Firstly, after the correction of the molecular contribution, the aerosol optical thickness (*AOT*) between a reference altitude z_0 and z is derived from the N_2-Channel by (e.g. *Royer et al.*, 2011)

$$AOT(z_0, z) = \frac{1}{(1+\eta_{aN})} \cdot \left| \ln\left(\frac{S_N(z_0)}{S_N(z)} \cdot \frac{\beta_N(z)}{\beta_N(z_0)} \cdot \exp\left((1+\eta_{mN}) \int_{z_0}^{z} \alpha_m(z') \cdot dz' \right)\right)\right| \quad (5)$$

The reference altitude z_0 can be taken in the upper or lower parts of the lidar profile. For this study, z_0 has been chosen above the aerosol layers, between 4 and 6 km amsl. Hence, the aerosol backscatter coefficient β_a can be directly calculated as

$$\beta_a(z)=\beta_E(z_0)\,{S_E(z)}\Big/{S_E(z_0)}\,\exp\left(2\cdot\left[\mathrm{sgn}(z-z_0)\cdot AOT(z_0,z)+\int_{z_0}^{z}\alpha_m(z')\cdot dz'\right]\right)-\beta_m(z) \qquad (6)$$

Secondly, the AOT can be used in two ways. The first one is via a regularization approach such as the Tikhonov regularization method (*Tikhonov and Arsenin*, 1977), from which the vertical profiles of LR and α_a are derived (e.g. *Royer et al.*, 2011) starting from the matrix form of :

$$AOT(z_0,z)=\left|\int_{z_0}^{z}LR(z')\cdot\beta_a(z')\cdot dz'\right| \qquad (7)$$

The second one is via an iterative algorithm using the *Klett* (1985) approach (*Chazette*, 2003; *Royer et al.*, 2011):

$$\alpha_a(z)=\overline{LR}\cdot\left(\frac{S_E(z)\,Q(z)}{\dfrac{S_E(z_0)}{\left(\beta_m(z_0)+\beta_a(z_0)\right)}+2\cdot\overline{LR}\cdot\int_{z}^{z_0}S_E(z')\,Q(z')\,dz'}-\beta_m(z)\right) \qquad (8)$$

where Q is the correction related to the differential molecular optical thickness calculated from the vertical profile of the molecular scattering coefficient:

$$Q(z)=\exp\left(2\left[k_f\,\frac{3\cdot\overline{LR}}{8\pi}-1\right]\int_{z}^{z_0}\alpha_m(z')\,dz'\right) \qquad (9)$$

The columnar mean lidar ratio $\overline{LR}$ that is derived from this second way corresponds to the value of $LR(z)$ weighted by the aerosol extinction coefficient profile between z and z_0.

The depolarization of the laser beam by aerosols is also a powerful tracer to contribute to the identification of the airmass origins. Taking into account that the channel transmissions are not pure in terms of polarization, the volume depolarization ratio (VDR) is explained as (e.g. *Chazette et al.*, 2012a)

$$VDR(z) \approx \frac{T_1^{//} \cdot S_{E2}(z)}{R_c \cdot S_{E1}(z)} - \left(1 - T_1^{//}\right) \cdot \left(1 - T_2^{//}\right) \quad (10)$$

$T_1^{//}$ and $T_2^{//}$ are the parallel transmissions of the total and cross-polarization channels. They were estimated before and after the experiment in laboratory on a specific optical bench (*Chazette et al*., 2012a). The cross-calibration coefficient R_c can be assessed by normalizing the lidar signals obtained in a "clean" atmospheric volume with negligible aerosol content:

$$R_c \approx \frac{S_{E2}(z) \cdot T_1^{//}}{S_{E1}(z)\left[\left(1 - T_1^{//}\right) \cdot \left(1 - T_2^{//}\right) + VDR_m\right]} \quad (11)$$

where the molecular volume depolarization ratio (VDR_m) was taken equal to 0.3945% at 355 nm following *Collis and Russel* (1976). Therefore the particulate depolarization ratio (*PDR*) is computed from

$$PDR(z) = \frac{\beta_m(z) \cdot \left(VDR_m - VDR(z)\right) - \beta_a(z) \cdot VDR(z) \cdot \left(1 + VDR_m\right)}{\beta_m(z) \cdot \left(VDR(z) - VDR_m\right) - \beta_a(z) \cdot \left(1 + VDR_m\right)} \quad (12)$$

2.3 Experimental sites

To ensure its mobility, WALI was embedded onboard the Mobile Aerosol Station van (*Chazette et al.*, 2005) also equipped with a VAISALA 200 probe mounted on a mast at ~10 m from the surface. Different experimental sites have been considered to calibrate and test WALI under field conditions. The first one is close to the Paris area at ~30 km South of Paris (48°42'50" N and 2°14'44" E). It is situated east of the Trappes meteorological station where rawinsoundings are performed twice daily. The second one is close to Montpellier (43° 37' 14" N and 4° 4' 11" E) in the South of France close to the Mediterranean coast. This site has been selected for the opportunity of launching a simultaneous rawinsounding with the lidar measurements without problem for the air traffic. The third site is the one selected to conduct the HyMeX/IODA-MED fall campaign in 2012 and the ChArMEx summer campaign in 2013. Shown in Figure 3, it is situated on the Balearic island of Menorca (Spain) to catch the water vapor amount before the airmasses reach the Spain and French coasts. The lidar-van was operated from a site close to Ciutadella (western part of the Menorca island, 39°60'00" N and 3°50'20"E) for HyMeX and close to Mahon (eastern part of the Menorca island, 39°49'32" N and 4°12'30"E) for ChArMEx. Rawinsounding were performed from Palma de Majorca (Majorca Island) at ~100 km southwest from the lidar location. A dedicated calibration flight was also performed over Mahon in the eastern part of the Menorca Island, at about 40 km east of Ciutadella. The main experimental period took place between September 10^{th} and October 30^{th} 2012.

3 Lidar calibration to retrieve the WVMR

As previously discussed, the vertical profile of the WVMR is retrieved using the ratio between the H_2O-Raman and N_2-Raman return signals. Nevertheless, this retrieval is subject to the prior assessment of both the calibration constant K and the overlap factor ratio ξ. Because of the uncertainties on the Raman backscatter cross-section and the difficulty to exactly characterize the optical transmission of the entire lidar detection system, the calibration has been performed comparatively to simultaneous vertical sounding using a well-qualified meteorological probe. K is first assessed using the upper part of the rawinsounding profile and ξ is then retrieved from the lower part (below 0.8 km amsl). The calibration adjustments have been computed using the minimum of the mean square deviation between the lidar and the rawinsounding profiles. Note that *Vaughan et al.* (1988) used a calibration on optical bench of each optical element leading to a final precision of 12% on the WVMR.

For the same purpose, atmospheric water vapor profiles have been monitored in the Paris area, in the Southeast of France, and at Menorca before, during and after the HyMeX

/IODA-MED campaign of the September-October 2012 (www.hymex.org). The calibration procedure has been conducted followings 3 chronological steps. 1) Lidar-derived WVMR profiles have been compared with specific nighttime rawinsoundings carried out by Meteo-France on September 1st and October 27th 2012 close to Paris and Montpellier, respectively. Hence, both K and ξ have been assessed. 2) Due to the difference of photomultipliers high voltage *(HV)* used during nighttime (950 and 1000 V for the N_2- and H_2O-channels, respectively) and daytime, a specific calibration function has been derived to allow continuity between the lidar measurements performed during night- and daytime, as K evolved against *HV*. 3) Independent rawinsoundings have been used to validate the previous calibrations using day- and night-time measurements performed from air-borne platforms equipped with VAISALA probes. These checks have been made before, during and after the campaign. Note that the WALI final vertical resolution has been fixed to 50 m for this calibration exercise.

Calibration. The rawinsounding performed near Montpellier was close to the lidar-van (~100 m), and is thus considered the most relevant mean to calibrate the lidar. It has been performed on October 30th 2012 during nighttime at 22:00 local time (LT). The result after calibration with $K = 0.066$ is given in Figure 4. The presence of clouds, highlighted on the elastic range-corrected lidar signal S_{355}, prevents us from verifying the agreement between the instruments over 1.6 km amsl. The standard deviation (std) between the lidar- and rawinsounding-derived WVMR is 0.13 g/kg (~2.3%). On the same figure, the rawinsounding station of Trappes has also been used to test the calibration with the same value $K = 0.066$ for a measurement performed in the Paris area (Palaiseau). The agreement is very good under 2 km amsl with a std of 0.2 g/kg as the lidar-van was downwind from the station. Over 2 km the discrepancy increases with a std close to 0.5 g/kg. The presence of mid-altitude clouds can explain the difference between lidar and rawinsounding above 2.5 km amsl.

High voltage variation during daytime. The diurnal evolution of the calibration coefficient *K* has been measured by two specific experiments over Menorca during the fall of 2012. The result is shown Figure 5 against the HVs of the N_2- and H_2O-Raman channels. During daytime the HVs were close to 850 and 650 V for the N_2- and H_2O-Raman channels, respectively. With such values *K* significantly increases to reach ~1. This calibration has been tested by measuring in the same airmass for HVs from 650 to 1000 V. Moreover, two areas (Menorca and Paris) with different WVMR have been considered as shown in Figure 6. The results are in good agreement with a std between 0.2 and 1 km amsl of ~0.8 and ~0.5 g/kg for Menorca and Paris, respectively. Note that the use of lower HVs leads to a decrease in the accessible altitude range because a lower PMT gain, chosen to avoid saturation by sky background light, decreases the signal to noise ratio.

Validation using independent rawinsoundings. The validation of the previous calibration has been carried out using measurements from balloon and aircraft. Figure 7 gives comparisons between WVMR retrieved from lidar and rawinsounding over the same previous sites of the Paris area, before, and several months after the IODA-MED campaign. The first (second) one is during nighttime (daytime). On September 5^{th} 2012 the lidar and rawinsounding comparison leads to a std of 0.83 g/kg for WVMR between 0.3 and 5 km amsl. The stronger discrepancy is mainly due to the airmass variability in the lower part of the profile. The agreement is significantly better on February 19^{th} 2013, with measurements performed during daytime. The std is equal to 0.29 g/kg between ~0.5 and 1.2 km.

A specific flight was performed above Mahon on October 27^{th} 2012 between 08:30 and 09:30 LT. The meteorological probe used on the plane was a VAISALA PTB110-Veriteq SP2000. It delivers the thermodynamic temperature with an uncertainty of 0.15 K, the pressure with an uncertainty of 0.6 hPa and the relative humidity with a relative uncertainty of

5% for the atmospheric conditions encountered in the low and middle troposphere. This leads to an absolute uncertainty of 0.67 g/kg on the WVMR. As shown in Figure 8, when compared to the lidar-derived WVMR, the std is 0.55 g/kg for altitudes between 0.2 and 1.2 km amsl, which is close to the error bars. Note that for the lidar, the std is also due to the atmospheric fluctuations during a diurnal average of one hour. Nighttime comparison with the rawinsounding of Palma de Majorca leads to a similar std of 0.48 g/kg. Figure 8 also includes comparison to operational modeling. The first output is from ECMWF (European Center for Medium-Range Weather Forecasts, www.ecmwf.int) analyses. The 9 closest grid points from Ciutadella have been considered, showing that the WVMR below 2 km is not fluctuating much with a std of 0.22 g/kg. The second model is AROME WMED whose WVMR forecast has been extracted above the ground-based lidar location. It is a mesoscale model based on a three dimensional variational data assimilation system with a horizontal resolution of 2.5 km, centered over the western part of the Mediterranean basin for real-time and case-study uses. It has been developed for the preparation of the experimental HyMeX special observation period. It is derived from the operational version of the AROME model (*Seity et al.*, 2011) which is centered over France. Lateral boundary conditions are provided by the global model ARPEGE (Action de Recherche Petite Echelle Grande Echelle). As shown in Figure 8 and still for altitudes from 0.2 to 1.2 km amsl, the comparison to lidar-derived WVMR for this specific case leads to std of 0.51 and 0.81 g/kg for ECMWF and AROME-WMED, respectively.

4 Error estimation

The different sources of uncertainty playing a major role in both the WVMR and the aerosol optical properties retrievals will be analyzed in this section. For the latter, we will consider the results already published by Chazette et al. (2012b) showing the entire methodology for the same type of lidar.

The uncertainties in the determination of the WVMR are related to 3 main sources: (i) the shot noise characterized by the signal to noise ratio (SNR_λ) of the lidar system, (ii) the calibration related to rawinsoundings, and (iii) the molecular and aerosol contributions. At the first order, the relative error ε_H on r_H is then given by

$$\varepsilon_H \approx \sqrt{\underbrace{\frac{1}{SNR_N^2}+\frac{1}{SNR_H^2}}_{\text{Shotnoise}}+\underbrace{\varepsilon_K^2+\varepsilon_\xi^2+\varepsilon_{HV}^2}_{\text{Calibration}}+\underbrace{\varepsilon_m^2+\varepsilon_a^2}_{Atmosphere}} \tag{13}$$

where ε_K, ε_ξ and ε_{HV} are the relative errors due to the calibration constant *K*, the overlap factors and the HV variation, respectively. The relative error associated to the spectral dependency of the extinction properties of molecules (aerosols) is given by ε_m (ε_a).

Shot noise. An accurate assessment of the shot noise contribution requires a precise characterization of the SNR. During nighttime such assessment is easier because the photon counting mode is active. In that mode, the associated standard deviation is the square root of the returned signal (*Measures*, 1984). An example is given on Figure 9 for a lidar signal acquired during the night of October 19th 2012 over Menorca with a vertical resolution of 15 m. The SNR is assessed for an average lidar profile over 1000 laser shots. The SNR for a larger number of laser shots *p* can be easily calculated knowing that it is proportional to $\sqrt{p}$. For a lidar signal averaged over 20 minutes (20000 laser shots) and using a Monte Carlo approach as in *Royer et al.* (2011), the uncertainty on the WVMR has been assessed as close to 0.08 (0.32) g/kg between 0 and 2 km (2 and 5 km) amsl. Figure 10 shows an example obtained during the same day for a representative WVMR vertical profile. Such uncertainties are a little lower than the deviations measured during the inter-comparison between lidar measurements and rawinsoundings.

Calibration. The relative uncertainty on the assessment of the overlap factor F is close to 3% and comparable to the previous assessment of 5% performed by *Chazette* (2003) when using the same approach. This leads to a relative uncertainty ε_{ξ} ~ 4% for altitudes between 0.3 and 0.80 km amsl. The accuracy and precision of the calibration constant K is closely related to the rawinsounding error that is directly linked to the type of radiosonde used for the rawinsounding. It is not easy to obtain such information from meteorological services. Fortunately some papers give the relative uncertainty for some meteorological probes (e.g. *Bock et al.*, 2009). The rawinsoundings performed over Palma de Majorca used VAISALA RS92 probes. A discussion on various VAISALA probes has been presented by *Agusti-Panareda et al.* (2009) following the African Monsoon Multidisciplinary Analysis (AMMA) field experiment in 2006 where numerous rawinsoundings were performed. They used the results of the WMO rawinsounding intercomparison experiment (*Nash et al.*, 2005) and the correction used by *Ciesielski et al.* (2003) for modeling applications. Such a correction has its own uncertainties as explained by *Wang et al.* (2002; 2008) because it does not take into account the solar heating effect, which affects the measurement during daytime. Moreover, the accuracy is affected by wet and dry biases. The magnitude of the humidity correction is up to 5% in the lower troposphere but can reach 20% in the upper troposphere. *Ferrare et al.* (1995) claim an accuracy of 2-3% with a precision of 2%. Such results have been confirmed by *Fujiwara et al.* (2003) and *Bock et al.* (2009) for VAISALA RS80 and RS92 probes. Accounting for all these considerations, we consider here that the relative error on the rawinsounding-derived WVMR is about 6% between 0 and 5 km amsl. Associated with the std between the lidar- and rawinsounding-derived WVMR, the calibration error is ε_K ~ 6.5%.

During daytime the effect of the HV variation has to be considered. The uncertainty is here mainly due to the atmospheric fluctuations during the HV scanning (~30 minutes). For mean lidar profiles of 1000 laser shots (Figure 6), the additional relative error is high (~10%). During daytime the number of laser shots has to be enhanced (60000 for 1 hour) and this uncertainty should decrease but it is difficult to quantify it. The easiest approach is to compare the lidar-derived WVMR to the one retrieved from daytime rawinsounding as shown in section 3. The calibration error is then around 7%.

Molecules and aerosols spectral dependencies. The third error source is negligible compared to the others. Indeed, the residual molecular contribution can be easily corrected using a climatologic model as in *Chazette et al.* (2003) leading to a very low uncertainty, i.e. less than 10^{-3} g/kg (0.3 g/kg when not corrected). The presence of aerosol layers leads to an error on r_H close to 0.01 g/kg (for A = 1). Nevertheless, such a contribution can be accounted for after the retrieval of the AOT derived from N_2-Raman channel.

Synthesis on the WVMR error. Taking into account all the main error sources, the relative VWMR error can be established for 3 different altitude ranges. During nighttime and for a temporal integrated sampling of 20 minutes (20000 laser shots), the relative error on the WVMR is ~8% within the first kilometer (0-0.8 km amsl). It reaches 11% between 2 and 5 km amsl. The smaller relative error is between 0.8 and 2 km amsl with a value of ~ 7%. Of course, the transitions are gradual and these values may change depending on the presence of more or less moist air masses in the middle troposphere. During daytime, the same relative error can be reached in the first kilometer but with 1 hour integration time. Actually, for operational purposes, the error on the WVMR can be calculated for each averaged profile knowing the SNR for both the N_2- and H_2O-channels. The main error source that could be reduced is the one due to the calibration, which is entirely dependent of both the rawinsounding measurement accuracy and precision.

Aerosol optical properties. Uncertainties on the retrieval of aerosol optical properties from similar detection channels have already been well discussed in the scientific literature (e.g. *Chazette et al.*, 2010; *Royer et al.*, 2011). For SNR > 20 as encountered with WALI, the relative uncertainty on the LR is ~5% (~10%) during nighttime (daytime). The relative uncertainty on the VDR and PDR are close to 10% for the encountered AOT > 0.2. The relative uncertainty on the AOT is less than 2%.

5 A case study analysis during the HyMeX campaign

WALI was operated during the 2012 fall campaign of the HyMeX program (Special Observing Period 1), between September 17th and October 27th. After presenting the lidar calibration and the assessment of the different error sources, we will present a study of a typical meteorological situation using a synergy between the WVMR and aerosols lidar measurements. As shown in Figure 11, an intense dust aerosol event was observed from October 17th to 20th. The VDR highlights two maxima, one on October 18th and the other on October 19th. This event has been sampled to follow its evolution along time. The different time periods considered are given in Table 2 with the corresponding dust layers and their main optical characteristics. The values of the WVMR are also given, showing a strong link between dust layers and significant water vapor contents.

Such an application uses the entire capability of the lidar but needs complementary information. Hence, exogenous modeling material has been used. Airmass backtrajectories have been computed to determine the corresponding transport routes (Figure 12) using the NOAA Hybrid Single Particle Lagrangian Integrated Trajectory (HYSPLIT) model (*Draxler and Rolph*, 2003) with 6-hourly archived meteorological data provided from the US National Centers for Environmental Prediction (NCEP) Global Data Assimilation System (GDAS) at the horizontal resolution of 0.5°. The altitude of the trajectory starting point was selected primarily from the lidar/in-situ observation of aerosol layer height. The WVMR along the airmass trajectory was retrieved by using the HYSPLIT model, which calculates the main meteorological parameters (i.e., temperature, relative humidity, pressure) along its trajectories. Note that the WVMRs given by the HYSPLIT model were in good agreement with those of balloon-borne data observed at an adjacent rawinsounding site for each time step of the trajectory (*Yoon et al.*, 2006). The outputs of the ECMWF re-analysis (http://www.ecmwf.int) have also been considered for illustrating the horizontal wind-field.

Before the arrival of the dust event, winds in the lower troposphere are southwesterly with low speeds, of the order of 2-5 ms^{-1} (Figure 13). They are associated with a low-pressure area situated in the South-western part of Ireland. They transport an aerosol layer above the marine boundary layer (MBL) (Figure 14) from the Spanish coast. In this layer, the mean LR (PDR) is ~ 77 sr (1%) as it can be expected for this type of pollution particles. The VDR is close to the value of its molecular contribution on the entire sampled atmospheric column (Figure 14), no desert dust aerosol is present. The higher values of the WVMR are located in the MBL (~9-10 g/kg), whose top altitude remained below 0.5 km amsl during all the experiment. A wet layer (>7 g/kg) is also present above the MBL where the polluted aerosols are trapped. From the airmass backtrajectories shown in Figure 12, it appears that this layer might be mainly off the Balearic Islands. Note that the rawinsounding from Palma de Majorca shows strong similarities with the lidar-derived WVMR profile between the surface and 5 km amsl (Figure 14). It is therefore very likely that the same air mass was sampled above the two sites. Above 2 km amsl the free troposphere is reached with a wet layer (WVMR ~2-3 g/kg) between 2 and 3.5 km amsl. The aerosol load in this layer is very low and non-depolarizing.

During the night of October 17th-18th 2012, the strong prevailing winds veer to the South, bringing relatively warm and humid airmasses from Sahara to Menorca, because of the presence of a cut-off over Ireland, which moves East during the event. Thus, Saharan airmasses penetrate over the Mediterranean from the Algerian coast (Figure 12 and Figure 13). The Saharan region is the world's major source of natural wind-blown mineral dust aerosol (e.g. *Hamonou et al.*, 1999; *Mona et al.*, 2012) and thus aerosol column burden may be enhanced when wind blows from the African coast. Indeed, the AOT (PDR) increases significantly from 0.1 to 0.18 (0.01 to 0.10) whereas the LR decreases to reach ~ 45 sr , which is a typical lidar ratio value for dust related aerosols (e.g. *Müller et al.*, 2007; *Mona et al.*, 2012). Stronger winds (> 10 $m.s^{-1}$) are linked to a higher WVMR (~10 g/kg) in the lower tropospheric layers. Dust aerosols are present in the MBL but the main dust layer is between 0.5 and 2.2 km amsl associated with r_H~6 g/kg that contrasts sharply with the content of the free troposphere. Similar observations can be made for the following day. The presence of important amounts of water vapor in the dust aerosol layers, between 4 and 6.7 g/kg, may contribute to maintain the particles in well-defined vertical structures along their transport for a longer period of time. The static stability of the layer can thus be enhanced as described by *Kim et al.* (2007; 2009). In return, dust plumes can act on the high precipitation events that occurred during the experimental period, by leading to the destabilization of the air masses coming from the sea that crossed the regions of Valencia and Tarragona (Spain) and upstream of Lourdes (France), where 24h accumulated rainfall of ~50 mm occurred on October 20th. Indeed, the presence of dust aerosol presence in the atmospheric column impacts the radiative balance and by this way modifies the vertical equilibrium by increasing the convection.

The atmospheric transport for October 18th and 19th is presented on Figure 12, Figure 13 and Figure 15. It confirms what has been described for the morning of October 18th. As the low moved eastward, the wind weakened and the event ended on October 20th (Figure 12 and Figure 15). The end of the event is associated with intense rainfalls related to the high humidity of the Saharan airmasses, which underwent subsidence over the Mediterranean Sea, while it caught water above the sea. Thus, the WVMR may have reached more than 15 g/kg at the ground level (Figure 14). These important amounts of water vapor are to put in parallel with the higher aerosol extinction coefficients, likely due to the hygroscopic growth of certain particle types. A mix of various aerosol types could be present in the MBL because the PDR remains high in this layer. During all the events, the PDR varied from 0.1 to 0.19 in the aerosol layers (Table 2). Such values are very close to the ones derived by *Müller et al.* (2007) with the Raman lidar POLIS in the frame of the Saharan Mineral Dust Experiment (SAMUM) with $PDR = 0.25 \pm 0.08$. By cons, the LR marks more significant differences between the aerosol layers. In the MBL, the LR derived from our study is found to be generally higher (~70 sr), which is in contrast to what can be expected for marine aerosols with a coarse mode of sea salt whose $LR \sim 25$ sr (e.g. *Flamant et al.*, 2000). Our derived LR value can be criticized for two reasons. Firstly, the altitude range of the MBL is more sensitive than the upper ones to the assessment of the lidar overlap function. Secondly, the boundary effects of the regularization method used to retrieve the aerosol optical properties during the night can strongly impact the derivation of the optical properties in the lower layers. Note that higher value of the LR was also retrieved on October 17th when no dust event occurred. Again, the result could be questionable because the AOT is low, close to 0.07, and the inversion procedure could not be well constrained. However, error studies show uncertainty of about 30% in such cases (e.g. *Chazette et al.*, 2012), which confirms the likely higher values of the LR in the MBL.

For the upper layers that contain more probably Saharan dust aerosols only, the LR ranges from 47 to 63 sr. It is significantly variable over the four days sampled. This indicates a high variability of aerosol optical properties and possibly of the particle nature. Different dust sources are activated along the days, as the low moves eastward, resulting in different types of dust particles transported. Moreover, human activities located close to the coast may also explain a part of this variability. The lidar-derived LR range can be retrieved from the literature. During the African Monsoon Multidisciplinary Analysis (AMMA), *Chazette et al*. (2007) found *LR* between 40 and 67 sr at 355 nm for the Harmattan dust layer above Niamey. During the same project, *Kim et al.* (2009) analyzed the CALIOP measurements and reported a value of $\overline{LR}$ ~36-38 sr at 532 nm. Note that the LR generally increases when wavelength decreases. *Cattrall et al.* (2005) also reported $\overline{LR}$ values close to 43 sr using sunphotometer measurements. *Dulac and Chazette* (2003) found a $\overline{LR}$ of 59 sr at 532 nm for a multilayer structure with desert, anthropogenic and marine aerosols over the Mediterranean. Moreover, *Mattis et al.* (2002) used the Raman lidar technique to measure the LR value of elevated dust layers during two episodes over Germany. They report *LR* values between ~50 and 77 sr at 532 nm. Again with a Raman lidar, Balis et al. (2004) give LR mainly between 45 and 55 sr at 355 nm for dust event over Thessaloniki.

6 Conclusion

Raman lidar systems are powerful tools for the atmospheric sampling of both water vapor and aerosols with high vertical resolution (between 15 and 50 m). Recent technology improvements of detectors, optics and electronics enable precise and reliable instruments and answer the increasing need to study the cycle of these atmospheric components. Aiming at new scientific and operational capabilities unavailable with current large instruments, the eye-safe transportable Raman lidar WALI has been developed with compact refractive telescopes for versatile measurements in the whole troposphere. This paper focused on the simultaneous retrieval of the WVMR and aerosol optical properties from the WALI instrument. It insists on the calibration procedure and on the error budget for deriving the WVMR.

The original design of the WALI system leads to very good capabilities in terms of low altitude overlap and WVMR retrieval during nighttime, that is to say, with an absolute deviation from rawinsoundings of less than 0.5 g/kg. The calibration procedure is the main error source for the lidar-derived WVMR, when dealing with a large SNR values. This error is very dependent on the rawinsounding accuracy and precision. It reaches 11% in the MBL and decreases to 7% below 5 km range for a temporal averaging of 20 minutes and a vertical resolution of 15 m. The precision of measurements can deteriorate very quickly thereafter due to the decreasing SNR with altitude. The determination of the water vapor is more difficult during daytime, but the measurements have been performed with the same uncertainty for altitude ranges below 1 km using a temporal averaging over ~1 hour.

The uncertainties linked to the retrieval of aerosol optical properties are comparable to the ones of previous Raman mobile lidars developed by our team with a relative error less than 10% for the LR or the PDR retrieval.

To demonstrate its performances for measuring the WVMR and the aerosol optical properties, the WALI system has been implemented in the Menorca Island during fall 2012 in the frame of the Mediterranean projects HyMeX and ChArMEx. It has allowed highlighting a strong event of desert dust aerosols associated with high water vapor contents between the 17^{th} and 20^{th} of October 2012. Both the LR and PDR attributed to dust particles are very variable but stay in the range of the variability reported in the literature, between ~45-63±6 sr and 0.1-0.19±0.01, respectively. These dust aerosol layers are associated with significant WVMR of ~4-6.7±0.4 g/kg, which may contribute to the important rain falls observed during this period over the Southwestern Europe.

Acknowledgments

This work was supported by the French Agence Nationale de la Recherche (ANR) via the IODA-MED project, the French space agency (CNES) and the Commissariat à l'Energie Atomique (CEA). We thank Dr. D.N. Whiteman for useful information for building the

WALI instrument. We also thank Dr. M. Sicard for its help for installing the lidar station on the Menorca Island. ECMWF data used in this study have been obtained from the ECMWF Data Server. Meteo-France is gratefully acknowledged for the rawinsounding data and the output of the AROME-WMED model. The authors would additionally like to thank the HyMeX program for the support of this work.

References

Agusti-Panareda, A., Vasiljevic, D., Beljaars, A., Bock, O., Guichard, F., Nuret, M., Lafore, J.-P., Andersson, E., Bechtold, P., Fink, A., Hersbach, H., Garcia Mendez, A., Ngamini, J.-B., Parker, D.J., Redelsperger, J.L., and Tompkins, A.: Radiosonde humidity bias correction over the West African region for the special AMMA reanalysis at ECMWF, *Quarterly Journal of the Royal Meteorological Society*, *135*, 640, pp 595-617, doi:10.1002/qj.396, 2009.

Ångström, A.: The parameters of atmospheric turbidity, *Tellus*, *16*, 64–75, 1964,

Ansmann, A., Riebesell, M., Wandinger, U., Weitkamp, C., Voss, E., Lahmann, W., and Michaelis, W.: Combined raman elastic-backscatter LIDAR for vertical profiling of moisture, aerosol extinction, backscatter, and LIDAR ratio, *Appl. Phys.*, B 55, *18*, 1992.

Balis, D.S., Amiridis, V., Nickovic, S., Papayannis, A., and Zerefos, C.: Optical properties of Saharan dust layers as detected by a Raman lidar at Thessaloniki, Greece, *J. Geophys. Res.*, *31*, L13104, doi:10.1029/2004GL019881, 2004.

Bock, O., and Nuret, M.: Verification of NWP model analyses and radiosonde humidity data with GPS precipitable water vapor estimates during AMMA, *Weather and Forecasting*, *24*, number 4, page 1085-1101,doi:10.1175/2009WAF2222239.1, 2009.

Boucher, O., and Anderson, L.: General circulation model assessment of the sensitivity of direct climate forcing by anthropogenic sulfate aerosols to aerosol size and chemistry, *J. Geophys. Res.*, *100*, D12, 26117-26134, 1995.

Bribes J. L., R. Gaufres, M. Monan, M. Lapp, and C. M. Penney (1976), Raman band contours for water vapor as a function of temperature, *Appl. Phys. Lett.*, *28*, 6, 336-337.

Bruneau, D., Quaglia, P., Flamant, C., Meissonnier, M., and Pelon, J.: Airborne Lidar LEANDRE II for Water-Vapor Profiling in the Troposphere. I. System description, *Appl. Opt.*, *40*, 3450-3461, 2001.

Draxler, R.R., and Rolph, G.D.: HYSPLIT (HYbrid Single-Particle Lagrangian Integrated Trajectory) Model access via NOAA ARL READY Website (http://www.arl.noaa.gov/ready/hysplit4.html). NOAA Air Resources Laboratory, Silver Spring, MD, 2003.

Cattrall, C., Reagan, J., Thome, K., and Dubovik, O.: Variability of aerosol and spectral lidar and backscatter and extinction ratios of key aerosol types derived from selected Aerosol Robotic Network locations, *J. Geophys. Res.*, *110*, D10S11, doi:10.1029/2004JD005124, 2005.

Ciesielski, PE, Johnson, R.H., Haertel, P.T., and Wang, J.: Corrected TOGA COARE sounding humidity data: Impact on diagnosed properties of convection and climate over the warm pool, *J. Climate*, *16*, 2370–2384, 2003.

Collis, R.T.H., and Russell, P.B.: Lidar measurement of particles and gases by elastic backscattering and differential absorption in Laser Monitoring of the Atmosphere, edited by Hinkley, E. D., pp. 71–152, Springler-Verlag, New York, 1976.

Chazette, P.: The monsoon aerosol extinction properties at Goa during INDOEX as measured with lidar, *J. Geophys. Res.*, *108*, 4187. 2003.

Chazette P., Couvert, P., Randriamiarisoa, H., Sanak, J., Bonsang, B., Moral, P., Berthier, S., Salanave, S., and Toussaint, F.: Three dimensional survey of pollution during winter in French Alps valleys, *Atmosph. Env.*, *39*, 1345-1047, 2005.

Chazette, P., Sanak, J.., and Dulac, F.: New Approach for Aerosol Profiling with a Lidar Onboard an Ultralight Aircraft: Application to the African Monsoon Multidisciplinary Analysis, *Environ. Sci. Technol.*, *41*, 8335–8341, 2007.

Chazette, P., Raut, J.-C., Dulac, F., Berthier, S., Kim, S-W., Royer, P., Sanak, J., Loaëc, S., and Grigaut-Desbrosses, H.: Simultaneous observations of lower tropospheric continental aerosols with a ground-based, an airborne, and the spaceborne CALIOP lidar systems, *J. Geophys. Res*, *115*, D00H31, 2010.

Chazette, P., Dabas, A., Sanak, J., Lardier, M., and Royer, P.: French airborne lidar measurements for Eyjafjallajökull ash plume survey, *Atmos. Chem. Phys.*, *12*, 7059-7072, doi:10.5194/acp-12-7059-2012, 2012a.

Chazette, P., Bocquet, M., Royer, P., Winiarek, V., Raut, J.-C., Labazuy, P., Gouhier, M., Lardier, M., and Cariou, J.-P.: Eyjafjallajökull ash concentrations derived from both lidar and modeling, *J. Geophys. Res*., *117*, D00U14, doi:10.1029/2011JD015755, 2012b.

Collis, R.T.H., and Russell, P.B.: Lidar measurement of particles and gases by elastic backscattering and differential absorption in Laser Monitoring of the Atmosphere, edited by: Hinkley, E. D., pp. 71–152, Springler-Verlag, New York, 1976.

Cooney, J. A.: Remote measurements of atmospheric water vapor profiles using the Raman component of laser backscatter, *J. Appl. Meteorol.*, *9*, 182-184, 1970.

Dulac, F., and Chazette, P.: Airborne study of a multi-layer aerosol structure in the eastern Mediterranean observed with the airborne polarized lidar ALEX during a STAAARTE campaign (7 June 1997), *Atmos. Chem. Phys.*, *3*, 1817–1831, 2003.

Fiocco G., and Smullin, L.D.: Detection of Scattering Layers in the Upper Atmosphere (60–140 km) by Optical Radar, *Nature*, *199*, 1275-1276, doi:10.1038/1991275a0, 1963.

Fiocco, G., and Grams, G.: Observations of the aerosol layer at 20 km by optical radar, *J. Atmos. Sci.*, *21*, 323-324, 1964.

Flamant C., Pelon, J., Chazette, P., Trouillet, V., Quinn, P., Frouin, R., Bruneau, D., Léon, J.F., Bates, T., Johnson, J., and Livingston, J.: Airborne lidar measurements of aerosol spatial distribution and optical properties over the Atlantic Ocean during an European pollution outbreak of ACE-2, *Tellus*, *52B*, 662-667, 2000.

Fujiwara, M., Shiotani, M., Hasebe, F., Vömel, H., Oltmans, S.J., Ruppert, P.W., Horinouchi, T., and Tsuda, T.: Performance of the Meteolabor ‘‘Snow White’’ chilled-mirror hygrometer in the tropical troposphere: Comparisons with the Vaisala RS80 A/H-humicap sensors. *J. Atmos. Oceanic Technol.*, *20*, 1534–1542, 2003.

Giorgi, F., and Lionello, P.: Climate change projections for the Mediterranean region, *Global and Planetary Change*, *63*, 90-104, 2008.

Hamonou, E., Chazette, P., Balis, D., Dulac, F., Schneider, X., Galani, E., Ancellet, G., and Papayannis, A.: Characterisation of the vertical structure of Saharan dust export to the Mediterranean basin, *J. Geophys. Res.*, *18*, 2257-2270, 1999.

Haywood, J.M., Roberts, D.L., Slingo, A., Edwards, J.M., and Shine, K.P.: General circulation model calculations of the direct radiative forcing by anthropogenic sulphate and fossil-fuel soot aerosol, *J. Clim.*, *10*, 1562, 1997.

Held, I.M., and Soden,B.J.: Water vapor feedback and global warming, *Annual Review of Energy and the Environment*, *25*, 441-475, DOI: 10.1146/annurev.energy.25.1.441, 2000.

IPCC, 2013: Climate Change 2013: The Physical Science Basis. Contribution of Working Group I to the Fifth Assessment Report of the Intergovernmental Panel on Climate Change [Stocker, T.F., D. Qin, G.-K. Plattner, M. Tignor, S.K. Allen, J. Boschung, A. Nauels, Y. Xia, V. Bex and P.M. Midgley (eds.)]. Cambridge University Press, Cambridge, United Kingdom and New York, NY, USA, 1535 pp.

Kim, S-W., Yoon, S-C., Jefferson, A., Won, J-G., Dutton, E.G., Ogren, J.A., and Anderson, T.L.: Observation of enhanced water vapor in Asian dust layer and its effect on atmospheric radiative heating rates, *Geophy. Res. Letters*, *31*, L18113, doi:10.1029/2004GL020024, 2004.

Kim, S.-W., Chazette, P., Dulac, F., Sanak, J., Johnson, B., andYoon, S.-C.: Transport and vertical structure of aerosols and water vapor over West Africa during the African monsoon dry season, *Atmos. Chem. Phys.*, *9*, 8017-8038, 2009.

King, L.V.: On the complex anisotropic molecule in relation to the dispersion and scattering of light, *Proceedings of the Royral Society of London*, Series 1, *104*, 333-357, 1923.

Klett, J.D.: Lidar inversion with variable backscatter/extinction ratios, *Appl. Optics*, *24*, 1638-1643, 1985.

Larson, T.V., and Taylor, G.S.: On the evaporation of NH4NO3 aerosol, *Atm. Env.*, *17*, 2489-2595, 1983.

Mattis, I., Ansmann, A., Müller, D., Wandinger, U., and Althausen, D.: Dual-wavelengthRamanlidar observations of the extinctionto- backscatter ratio of Saharan dust, *Geophys. Res. Lett.*, *29*, doi:10.129/2002GL014721, 2002.

Mattis, I., Siefert, P., Müller, D., Tesche, M., Hiebsch, A., Kanitz, T., Schmidt, J., Finger, F., Wandinger, U., and Ansmann, A.: Volcanic aerosol layers observed with multiwavelength Raman lidar over central Europe in 2008–2009, *J. Geophys. Res*., 115, D00L04, doi:10.1029/2009JD013472, 2010.

Measures, R.M.: Laser remote sensing: Fundamentals and Applications, *Wiley & Sons*, NewYork, 1984.

Melfi, S.H., Lawrence Jr., J.D., and McCormic, M.P.: Observation of Raman scattering by water vapor in the atmosphere, *Appl. Phys. Lett*., *15*, 295-297, 1969.

Melfi, S.H., Whiteman, D.N., and Ferrare, R.: Observation of atmospheric fronts using Raman lidar moisture measurements, *J. Appl. Meteorol.*, *28*, 789-806, 1989.

Mona, L., Liu, Z., Müller, D., Omar, A., Papayannis, A., Pappalardo, G., Sugimoto, N., and Vaughan, M.: Lidar Measurements for Desert Dust Characterization: An Overview, *Advances in Meteorology*, *2012*, doi:10.1155/2012/356265, 2012.

Müller, D., Ansmann, A., Mattis, I., Tesche, M., Wandinger, U., and co-authors: Aerosol-type-dependent lidar ratios observed with Raman lidar, *J. Geophys. Res.*, *112*, doi:10.1029/2006JD008292, 2007.

Nash, J., Smout, R., Oakley, T., Pathnack, B., and Kumosenko, S.: WMO Intercomparison of High Quality Radiosonde Systems, Vacoas, Mauritius, 2–25 February 2005, WMO report, February 2005 (http://www.wmo.int/pages/prog/www/), 2005.

Nicolet, M.: On the molecular scattering in the terrestrial atmosphere, *Planet. Space Sci*., 32, 1467–1468, doi:10.1016/0032-0633(84)90089-8, 1984.

Higdon, N.S., Browell, E.V., Ponsardin, P., Grossmann, B.E., Butler, C.F., Chyba, T.H., Mayo, M.N., Allen, R.J., Heuser, A.W., Grant, W.B., Ismail, S., Mayor, S.D., and Carter, A.F.: Airborne differential absorption lidar system for measurements of atmospheric water vapor and aerosols, *Appl. Opt.*, *33*, 6422-6438, 1994.

Penney, C.M., and Lapp, M.: Raman-scattering cross sections for water vapor, *J. Opt. Soc. Am.*, *66*, 422-425, 1976.

Raut, J.-C. and Chazette P.: Assessment of vertically-resolved PM10 from mobile lidar observations, *Atmos. Chem. Phys*., 9, 8617-8638, 2009.

Reichardt, J., Wandinger, U., Klein, V., Mattis, I., Hilber, B., and Begbie, R.: RAMSES: German Meteorological Service autonomous Raman lidar for water vapor, temperature, aerosol, and cloud measurements, Appl. Opt., 51, 8111-8131, doi.org/10.1364/AO.51.008111, 2012.

Rood, M.J., Covert, D.S., and Larson, T.V.: Hygroscopic properties of atmospheric aerosol in Riverside, California, *Tellus*, *39B*, 383-397, 1987.

Royer, P., Chazette, P., Lardier, M., and Sauvage, L.: Aerosol content survey by mini-N2-Raman lidar: Application to local and long-range transport aerosols, *Atmos. Environ.*, doi:10.1016/j.atmosenv.2010.11.001, 2011.

Sanchez-Gomez, E., Somot, S., and Mariotti, A.: Future changes in the Mediterranean water budget projected by an ensemble of regional climate models, *Geophys. Res. Lett.*, *36*, L21401, doi:10.1029/2009GL040120, 2009.

Seity, Y., Brousseau, P., Malardel, S., Hello, G., Benard, P., Bouttier, F., Lac, C., and Masson, V.: The AROME-France convective-scale operational model, *Mon. Weather Rev.*, *139(3)*, 976–991, doi:10.1175/2010MWR3425.1, 2011.

Tikhonov, A.E. and Arsenin, V.Y. Solutions of Ill-posed Problems. Wiley, 1977.

Turner, D.D., and Goldsmith, J.E.M.: Twenty-Four-Hour Raman Lidar Water Vapor Measurements during the Atmospheric Radiation Measurement Program's 1996 and 1997 Water Vapor Intensive Observation Periods, *J. Atmos. Oceanic Technol.*, *16*, 1062–1076, 1999.

Vaughan, G., Wareing, D.P., Thomas, L., and Mitev, V.: Humidity measurements in the free troposphere using Raman backscatter, *Q. J. R. Meteorol. Soc.*, *114*, 1471-1484, 1988.

Veselovskii, I.A., Cha, H.K., Kim, D.H., Choi, S.C., and Lee, J.M.: Raman lidar for the study of liquid water and water vapor in the troposphere, *Applied Physics B*, *71*, Issue 1, pp 113-117, DOI:10.1007/s003400000290, 2000.

Wang, J, Cole, H.L., Carlson, D.J., Miller, E.R., and Beierle, K.: Corrections of humidity measurement error from the Vaisala RS80 radiosonde – application to TOGA COARE data, *J. Atmos. Oceanic Technol.*, *19*, 981–1002, 2002.

Wang J, and Zhang, L.: Systematic errors in global radiosonde precipitable water data from comparison with ground-based GPS measurements, *J. Climate*, *21*, 2218–2238, 2008.

Whiteman, D.N., Melfi, S.H., and Ferrare, R.A.: Raman lidar system for the measurement of water vapor and aerosols in the earth's atmosphere, *Appl. Opt.*, *31*, 3068–3082, 1992.

Whiteman, D.N., Rush, K., Veselovskii, I., Cadirola, M., Comer, J., Potter, J.R., and Tola, R.: Demonstration Measurements of Water Vapor, Cirrus Clouds, and Carbon Dioxide Using a High-Performance Raman Lidar, *J. Atmos. Oceanic Technol.*, *24*, 1377–1388, 2007.

Yoon, S.-C., Kim, S.-W., Kim, J., Sohn, B-J., Jefferson, A., Choi, S.-J., Cha, D.-H., Lee, D-K., Anderson, T.L., Doherty, S.J., and Weber, R.J.: Enhanced Water Vapor in Asian

Dust Layer: Entrainment Processes and Implication for Aerosol Optical Properties, *Atmosph. Env.*, *40* (13), 2409-2421, 2006.

Table 1: Main technical characteristics of the WALI instrument.

Laser	Nd:Yag
Energy	60 mJ at 355 nm
Frequency	20 Hz
Reception channels	Elastic total 354.67 nm Elastic ⊥ 354.67 nm Raman-N_2 386.63 nm Raman-H_2O 407.5 nm
Reception diameters	15 cm
Field of view	~2.3 mrad
Full overlap	~300 m
Detector	Photomultiplier tubes
Filter bandwidths	0.2 - 0.3 nm
Vertical sampling	0.75 m (analog) 15 m (photon counting)
Vertical resolution	~30 m
Acquisition system	PXI technology at 200 MHz

Table 2: Analysis of the dust event of October 17th to 20th over Menorca: different dust layers and their LIDAR derived WVMR and aerosol optical properties for 7 different time periods. The main dust layers are highlighted in gray.

Date	Altitude range (km)	AOT at 355 nm (0.25 to 5 km)		$\overline{r_H}$ (g/kg)	$\overline{LR}$ (sr)		$\overline{PDR}$
17 00:00-03:00 LT	0.3-1.0	~0.07	0.04	8.8±0.6	74	67±8	0.01±<0.01
	2-3.5		<0.01	2.8±0.3		-	-
18 00:00-03:00 LT	0.3-0.5	~0.17	0.03	10.0±3	45	66±3	0.1±0.01
	0.5-2.0		0.09	6.4±0.4		47±6	0.1±0.01
18 10:30-14:30 LT	0.3-1	~0.38	0.06	7.9±2	59	-	0.15±0.02
	1.5-3		0.21	-		-	0.16±0.01
18 21:00-24:00 LT	0.5-1.5	~0.29	0.09	5.8±0.4	71	69±7	0.16±0.01
	1.5-4		0.12	4.1±0.4		63±2	0.19±0.01
19 00:00-03:00 LT	0.5-1.5	~0.38	0.09	6.3±0.8	63	58±8	0.12±0.01
	2-3.5		0.12	4.0±0.2		53±2	0.18±0.01
19 03:00-06:00 LT	0.3-1.0	~0.46	0.07	7.2±2	60	69±15	0.15±0.02
	1.0-3.5		0.32	4.7±1		60±4	0.18±0.01
20 00:00-03:00 LT	0.5-1.0	~0.14	0.03	7.6±0.2	53	59±7	0.10±0.01
	1.0-2.5		0.07	6.7±0.5		40±2	0.10±0.01

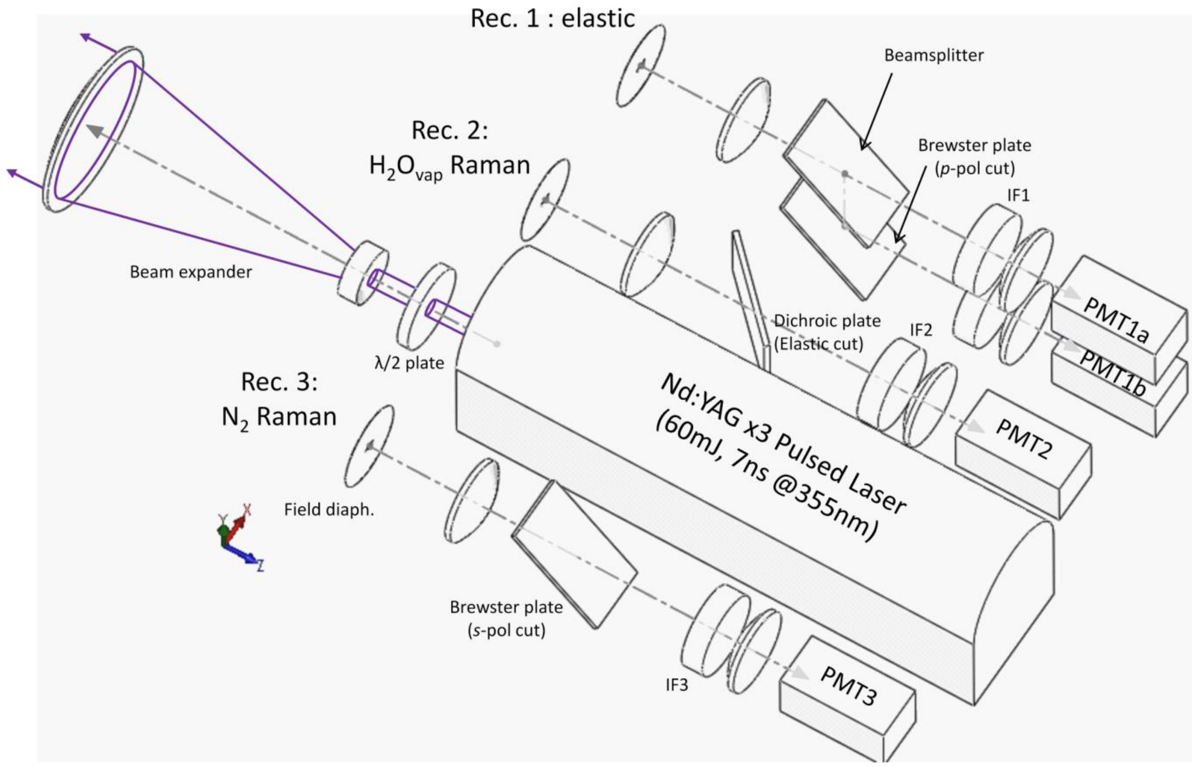

Figure 1: Schematic representation of the WALI. The receiver refractive telescopes, located on each path before the field diaphragm, were omitted for clarity. The 3 separate detection boards are highlighted with their main components. The emission size is adapted using a beam expander to fulfill eye-safe conditions. The elastic (354.67 nm) detection board is composed of 2 polarization channels: total and cross-polarized. The separation of the radiation over the 2 channels is done using a beam-splitter plate. The N_2-Raman detection board (386.63 nm) is equipped with a 386.63 nm working-wavelength Brewster plate to get rid of half of the sky-background. The H_2O-channel detection board (407.5 nm) is equipped with an additional dichroic plate to ensure a total rejection of the fundamental radiation at 354.67 nm.

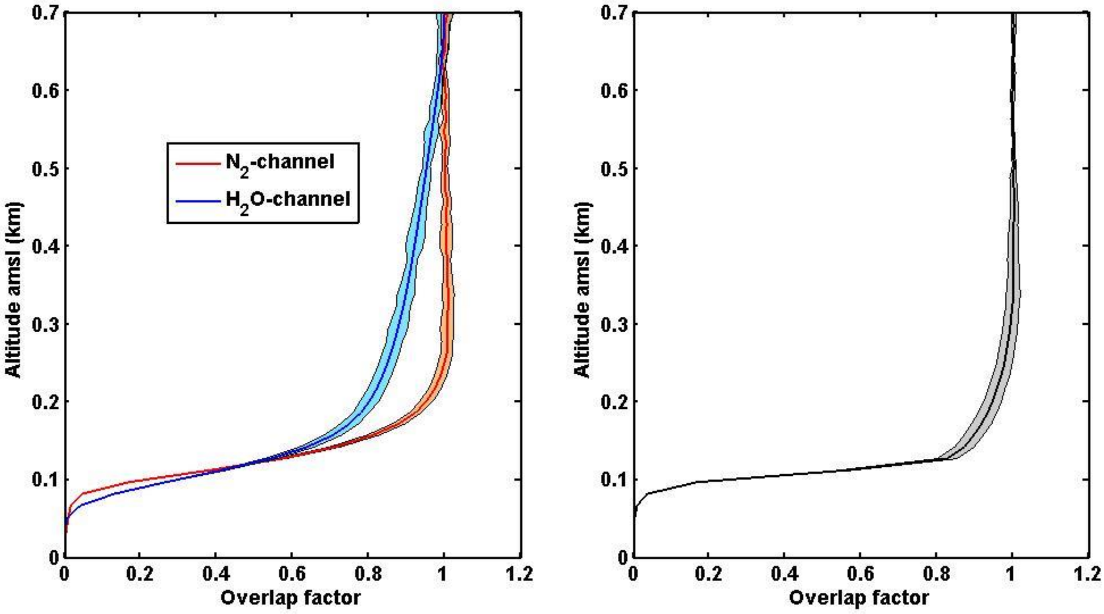

Figure 2: WALI Overlap factors for the N_2-, H_2O-channels (left) and elastic channel (right) as experimentally measured. The colored areas represent the standard deviations of the overlap factors.

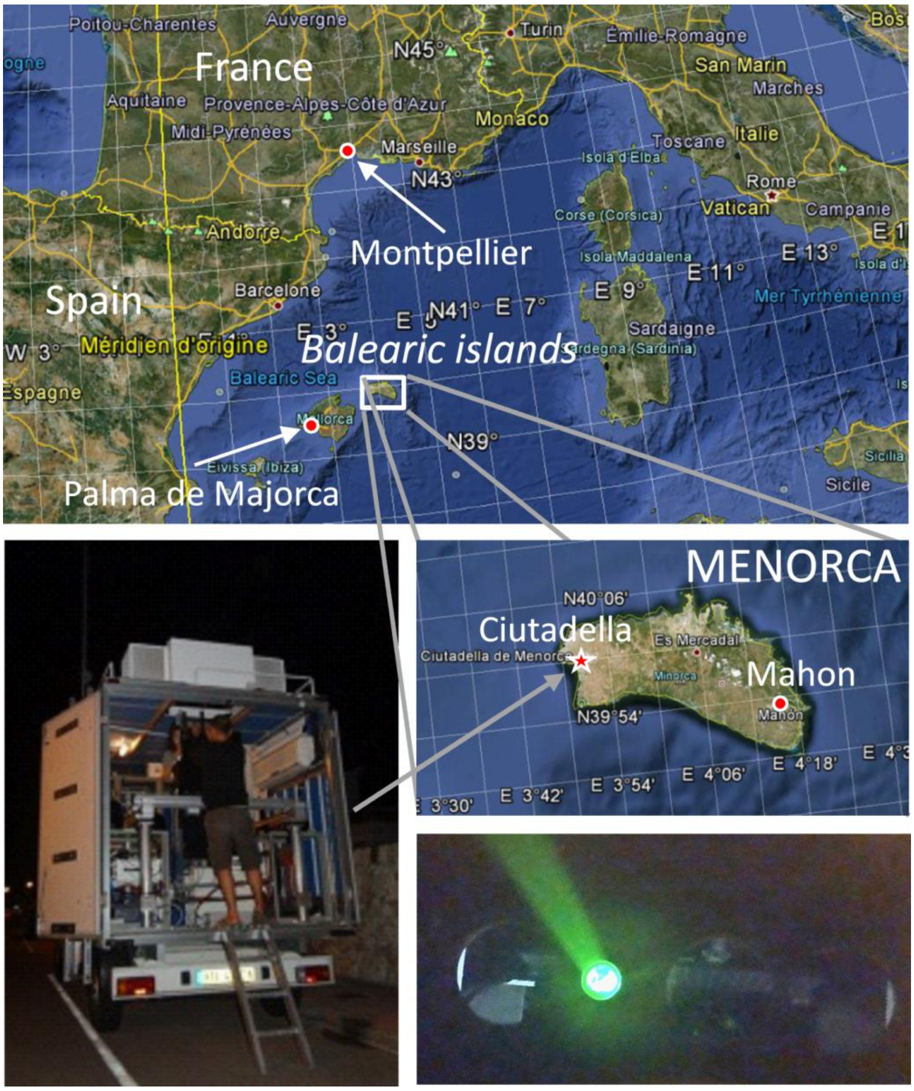

Figure 3: Southern experimental sites selected for both the HyMeX/IODA-MED and the ChArMEx campaigns. The ground-based lidar-van is shown on the bottom-left. The main experimental sites are indicated on the map (courtesy of Google Inc.).

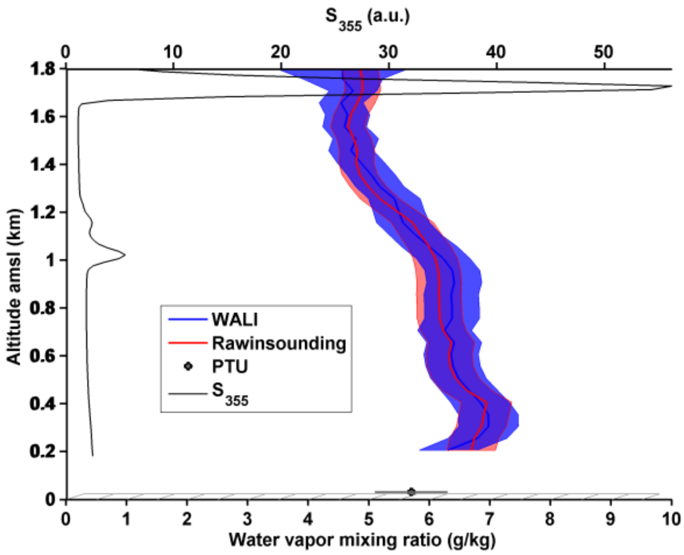

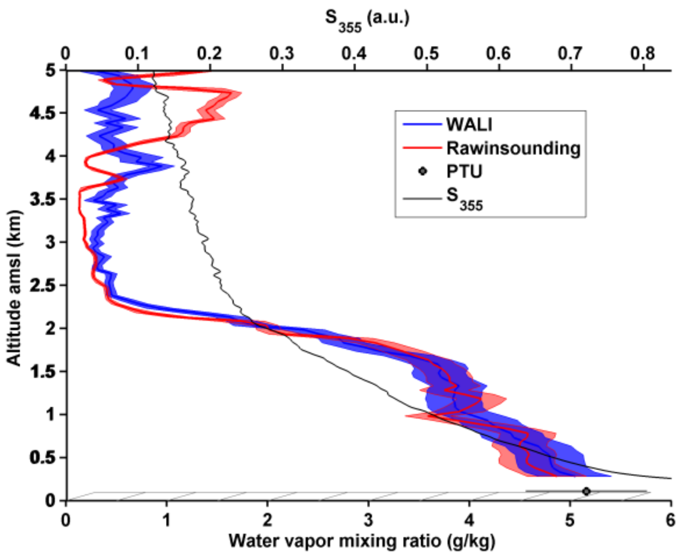

Figure 4: WALI WVMR retrieval calibration by comparison to rawinsounding: in Montpellier on October 30th 2012 22:00 LT (up) and in Palaiseau (Paris area) on September 1st 2012 01:00 LT (down). The red (blue) areas give the standard deviations around the VWMR mean value derived from the rawinsoundings (lidar). PTU stands for the ground-based measurements at ~10 m from the surface.

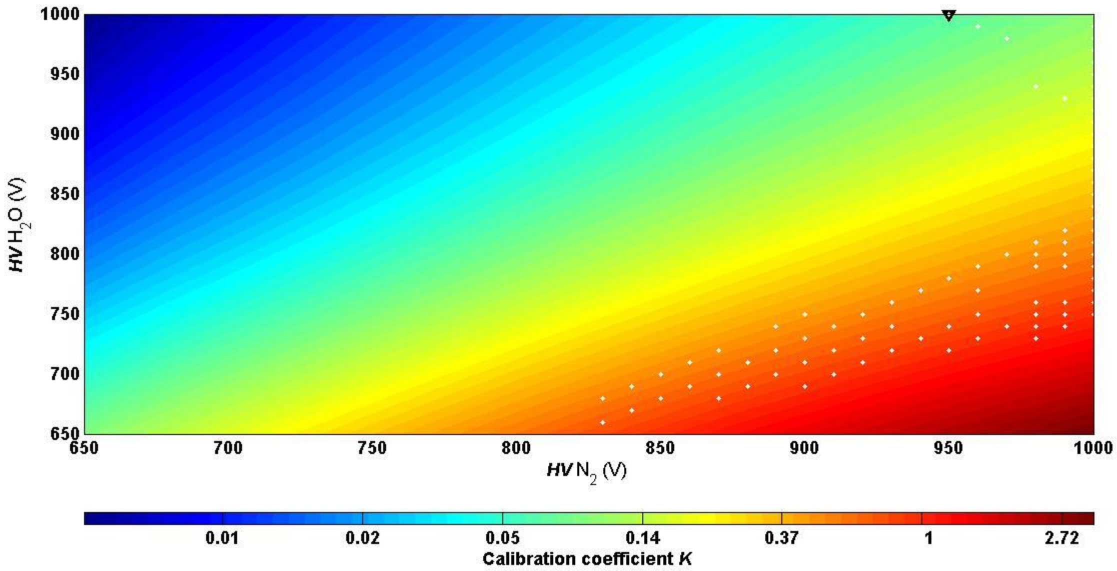

Figure 5: Photomultiplier High Voltage (HV) dependent calibration coefficient K with respect to N_2 channel and H_2O channel HVs. The black triangle locates the usual night-time setup. The white dots represent the automatic selected HVs during daytime.

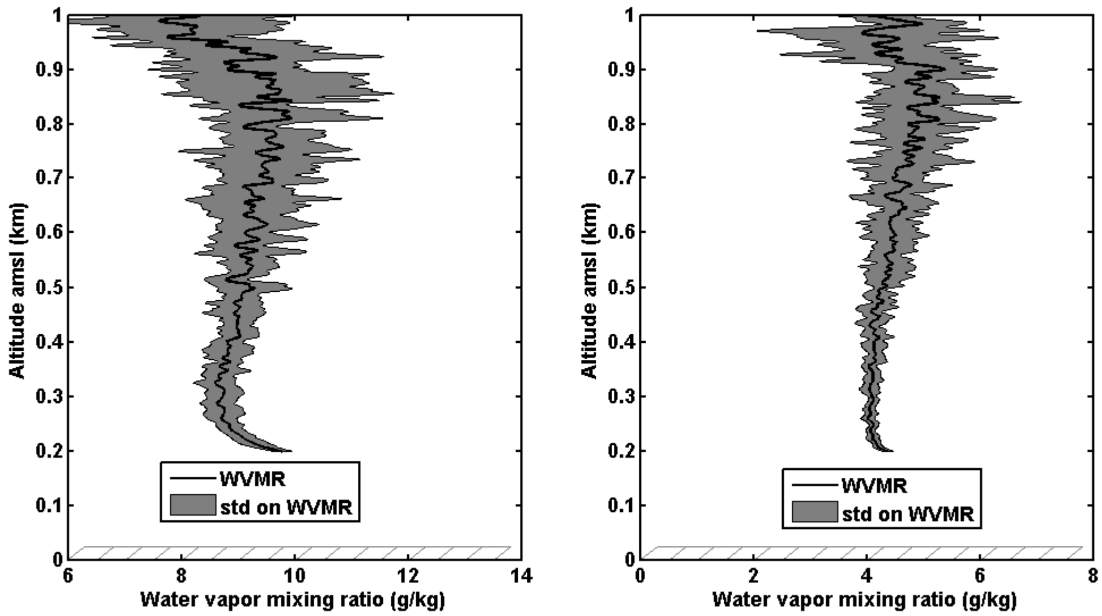

Figure 6: Test of the WVMR calibration for HVs varying between 650 and 1000 V over the Menorca site (on October 21st 2012 from 20:00 to 20:30 LT) (left) and the Paris area (November 8th 2012 from 17:45 to 18:15 LT). Both the mean value and the standard deviation (gray area) computed on the WVMR retrieval are derived from lidar profiles associated with the different HVs.

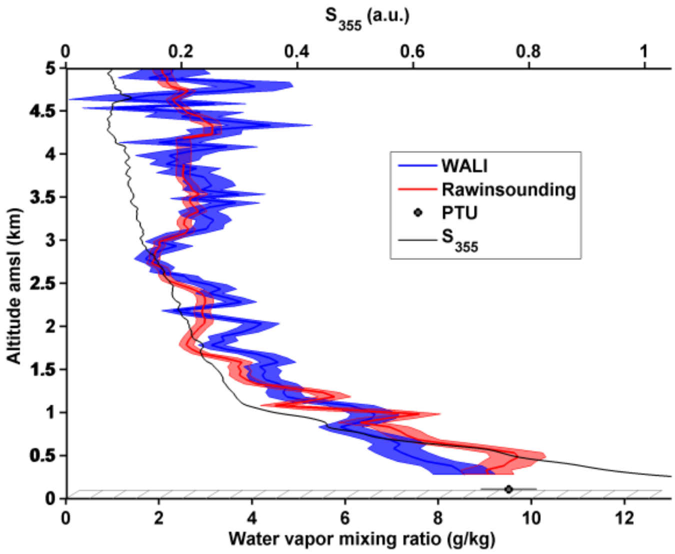

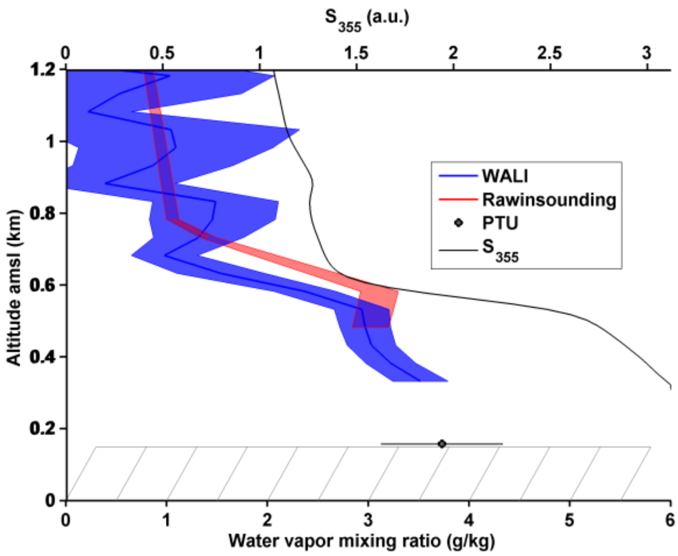

Figure 7: Calibration validation by comparing lidar derived WVMR to rawinsounding in Paris area before IODA-MED experiment on September 5th 2012 00:50-01:15 LT (up) and after IODA-MED on February 19th 2013 12:30-13:00 LT (down). The red (blue) areas give the standard deviations around the VWMR mean value derived from the rawinsoundings (lidar). PTU stands for the ground-based measurements at ~10 m from the surface.

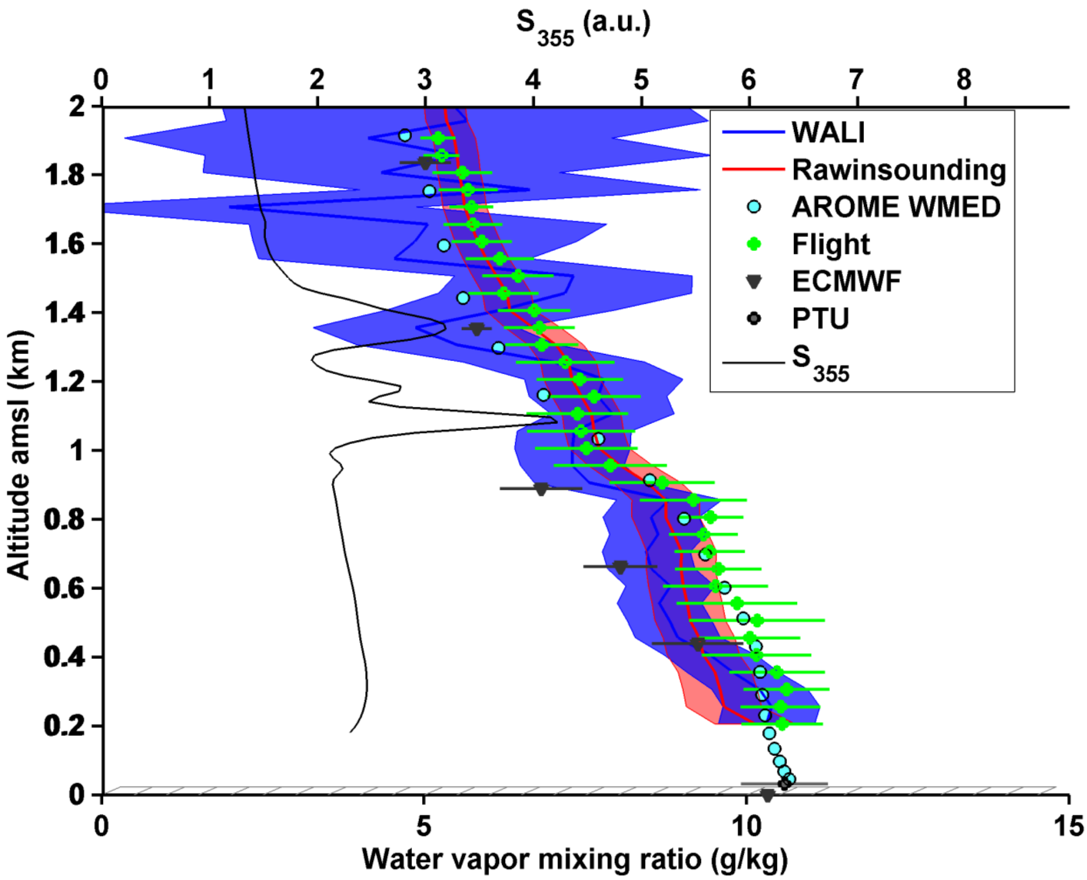

Figure 8: Comparison of lidar-derived WVMR in Ciutadella to airborne in-situ measurements during a flight over Mahon (with green error bars), Palma rawinsounding, ECMWF (with the standard deviation for the 9 closest modeled profiles from the lidar location) and AROME-WMED model outputs on October 27th 2012 08:30 to 09:30 LT. The gray (blue) areas give the standard deviations around the WVMR mean value derived from the rawinsoundings (lidar). PTU stands for the ground-based measurements at ~10 m from the surface.

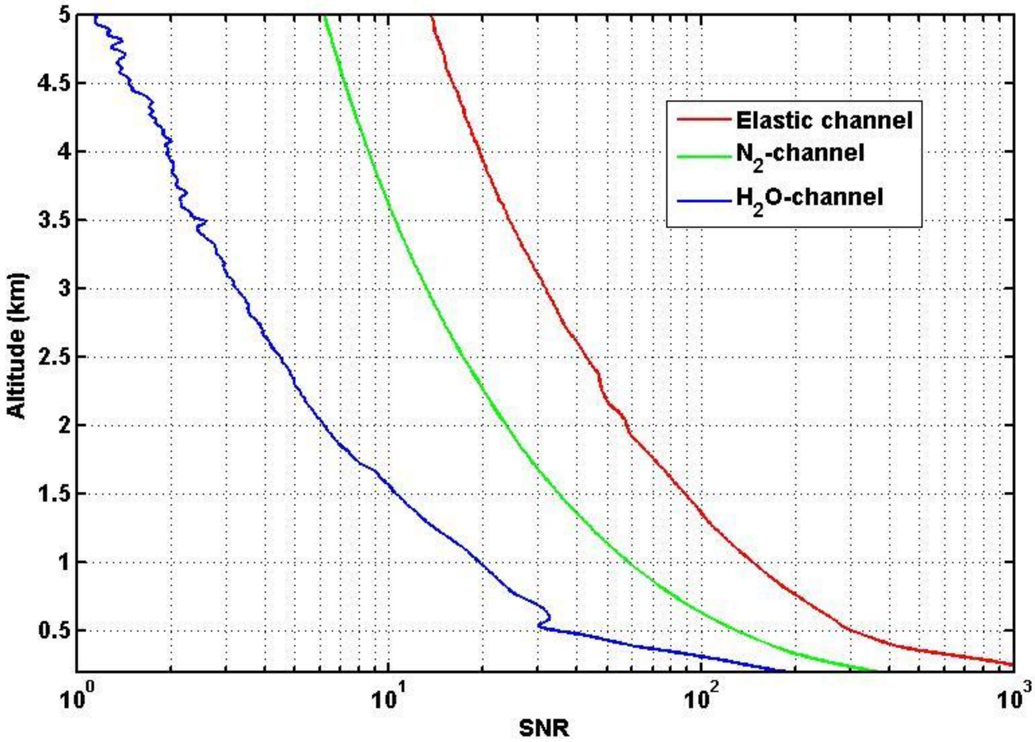

Figure 9: WALI Signal to Noise Ratio (SNR) as a function of altitude for 3 channels (Elastic, N_2-Raman and H_2O-Raman) for a 1000 shots average lidar profile obtained on October 19th 2012 during nighttime over Menorca.

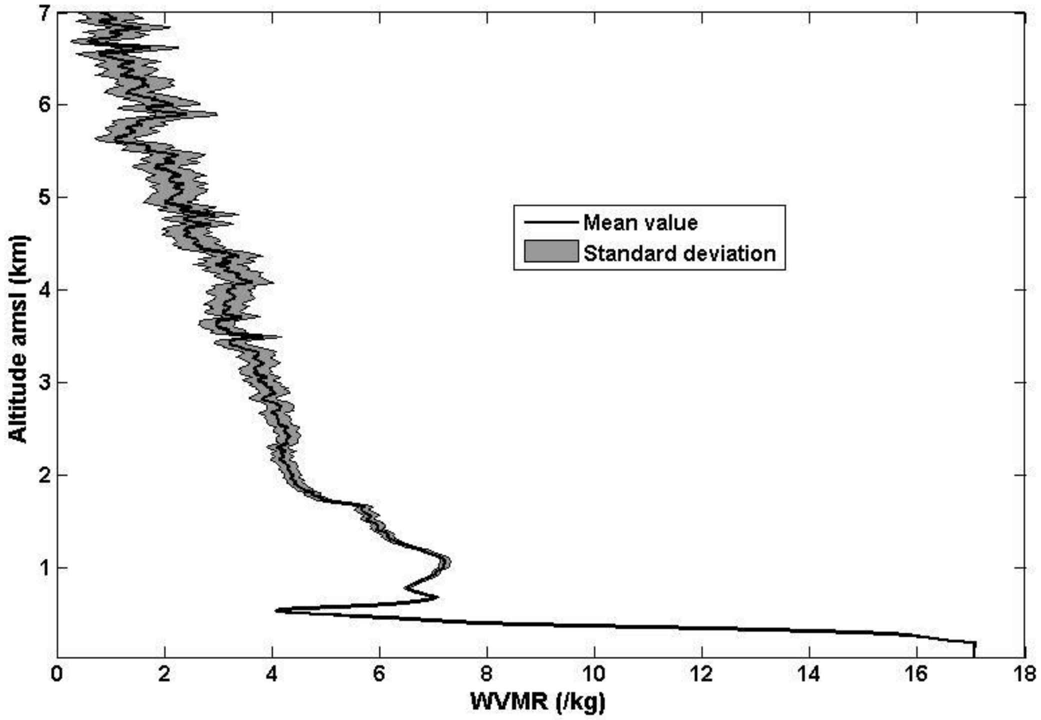

Figure 10: WALI derived-WVMR profile (black) and its associated standard deviation (gray) averaged over 20 minutes (20000 laser shots) during the night of October 19th 2012 over Menorca.

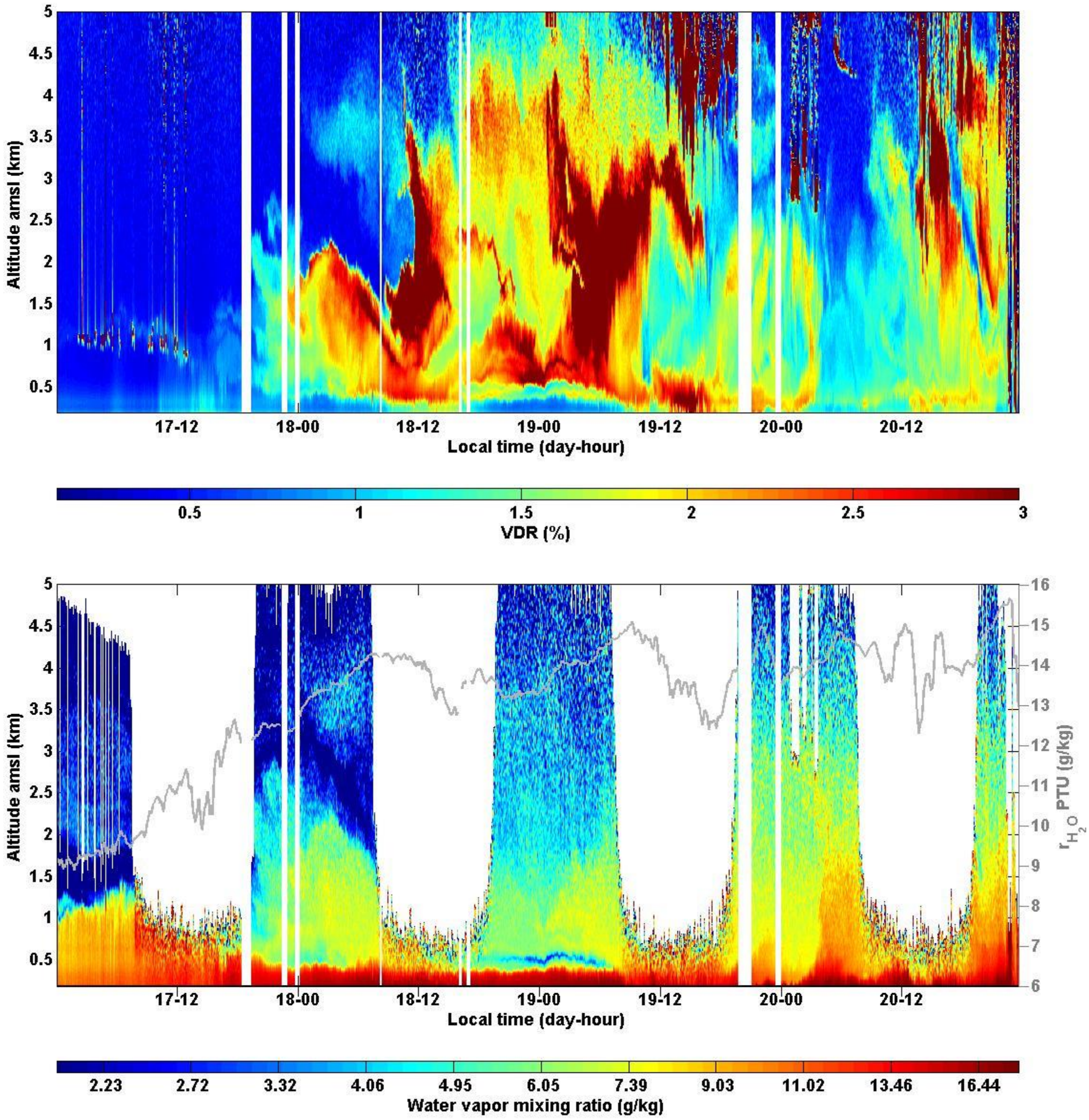

Figure 11: WALI lidar derived VDR (up) and WVMR (down) from October 17th to October 20th over Menorca. The gray solid line represents ground-based WVMR measurements from a meteorological probe at ~10 m from the surface.

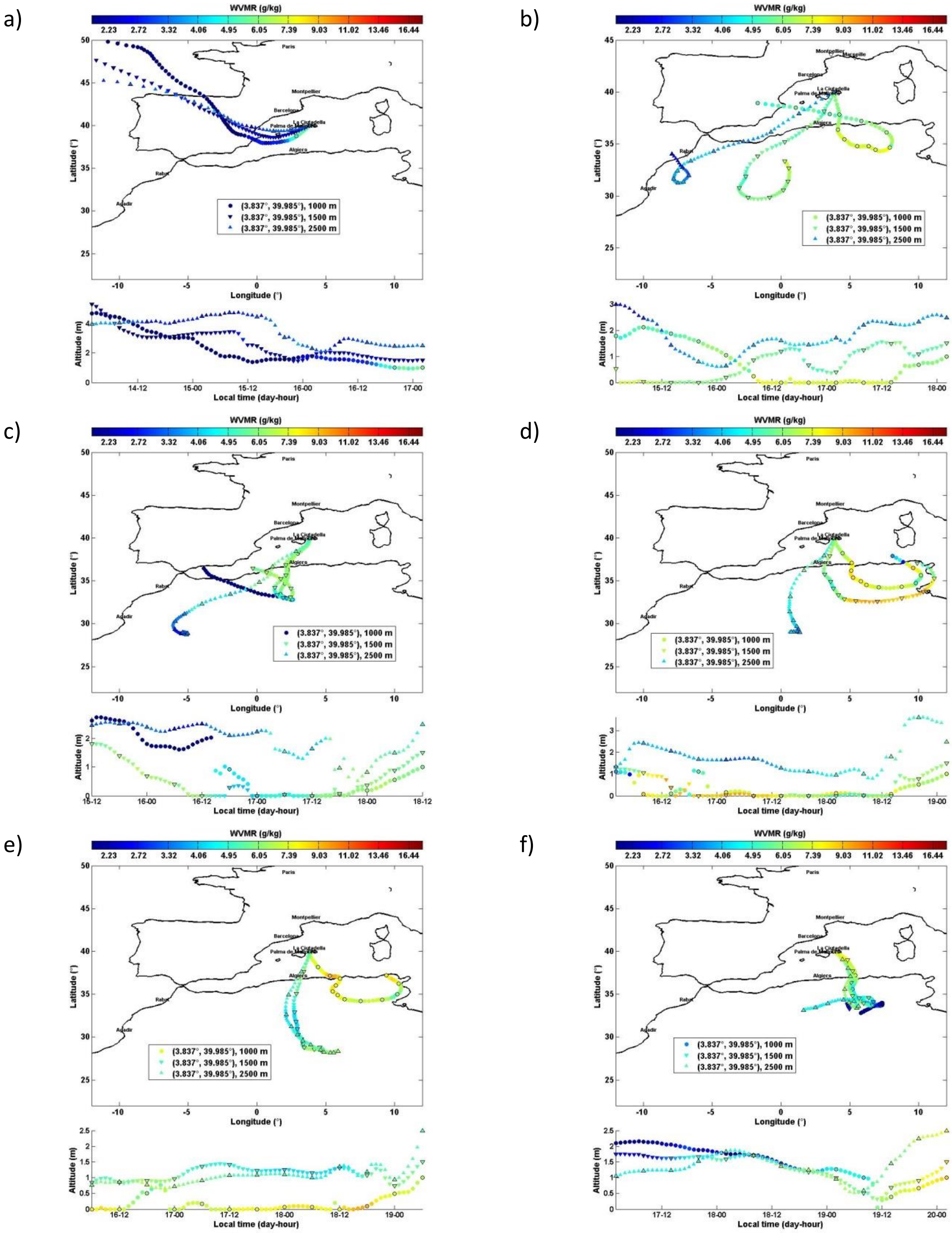

Figure 12: Backtrajectories between the 17th and 20th October 2012. They have been computed using the Hysplit model (courtesy of NOAA Air Resources Laboratory; http://www.arl.noaa.gov). The wind fields are from GDAS (Global Data Assimilation System, http://www.ncep.noaa.gov/) at the horizontal resolution of 0.5°. The terminal location of the

air masses is the site of Ciutadella for the altitudes: 1, 1.5 and 2.5 km amsl. The color bar represents the WVMR along the trajectories.

a)
b)
c)

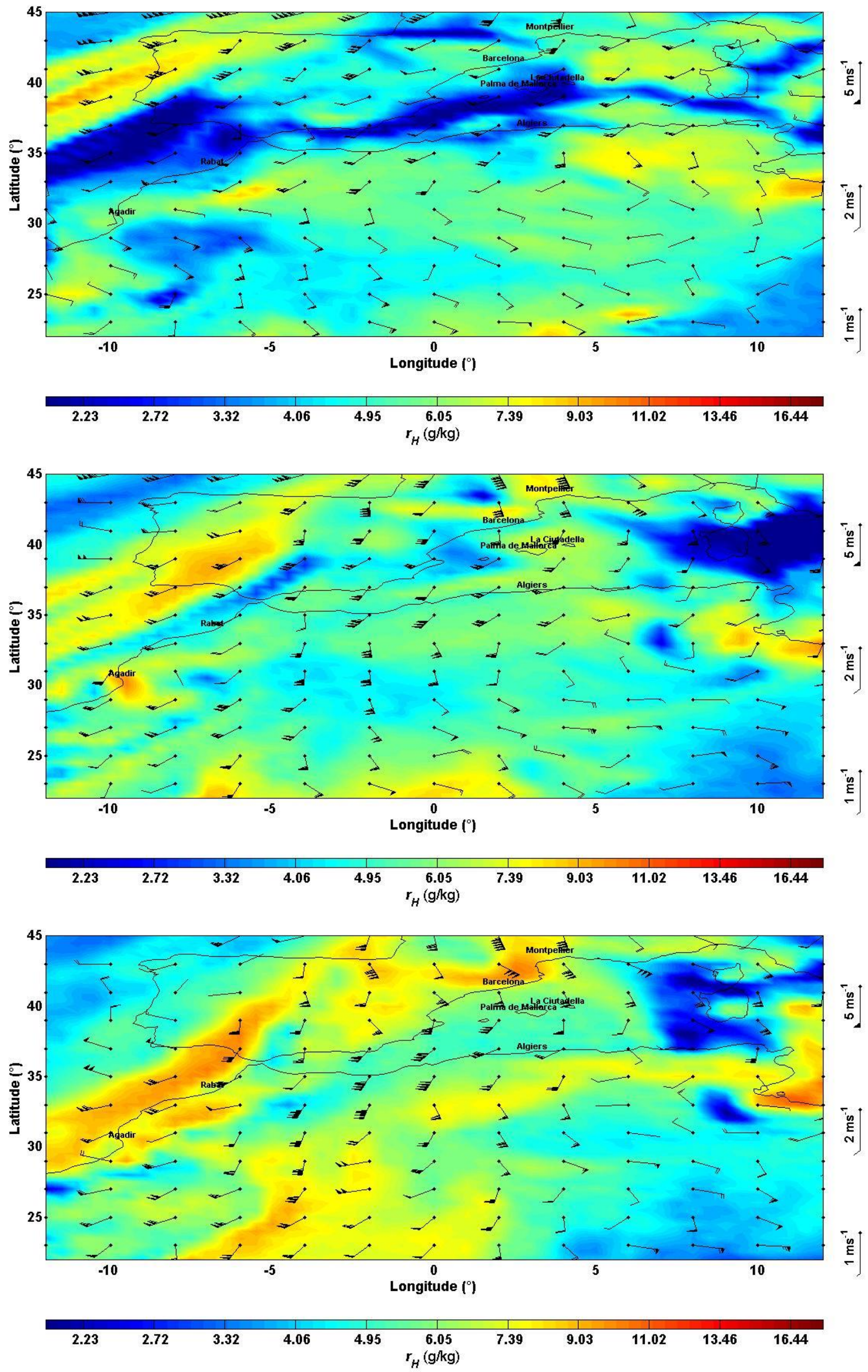

Figure 13: Wind-field (wind barbs) and WVMR (r_H) (color plot) from ECMWF OPERA 0.5° horizontal resolution analysis at 850 hPa level for October 17th at 02:00 LT (a), October 18th 02:00 LT (b), and October 18th 14:00 LT (c).

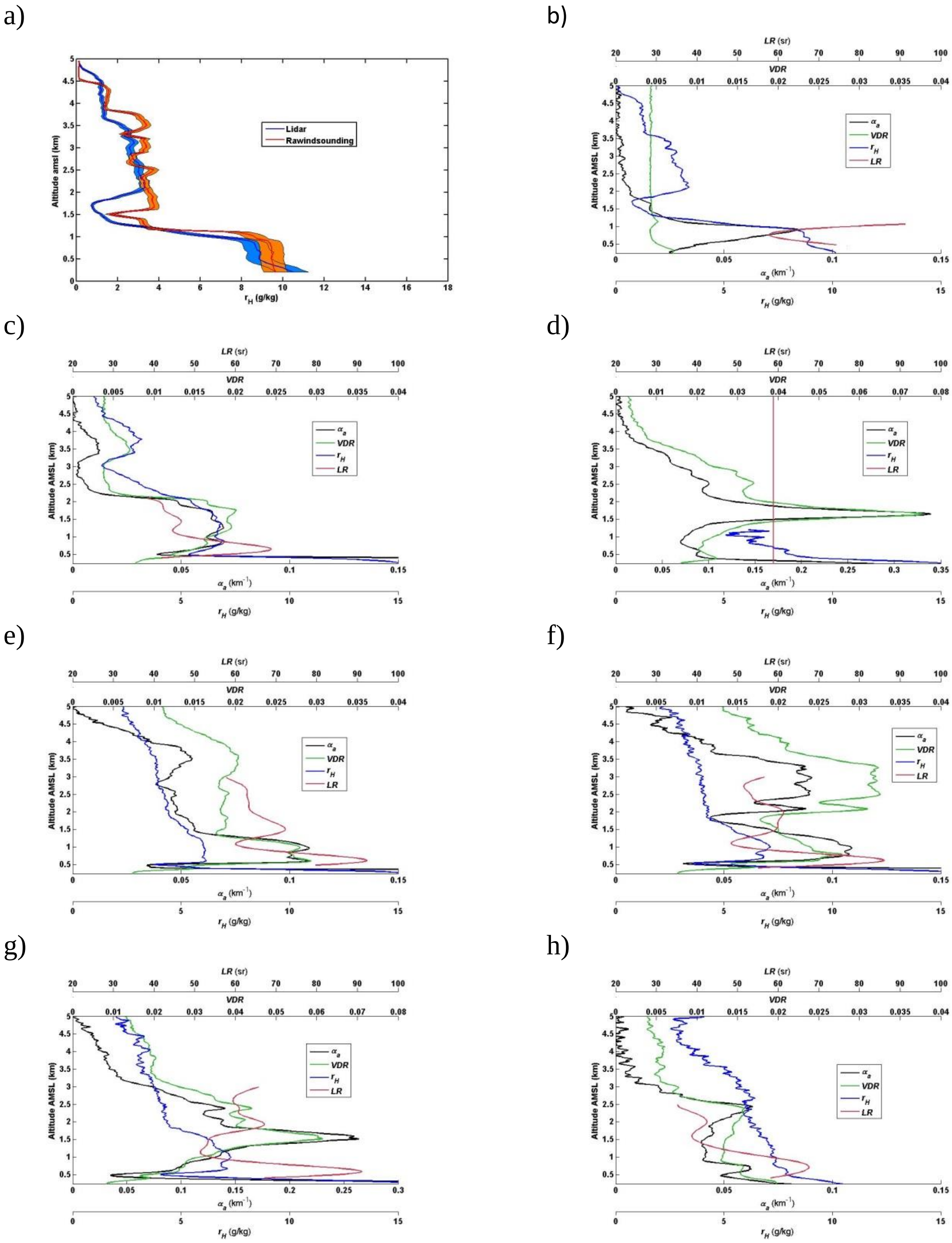

Figure 14: Comparison between lidar derived WVMR (r_H) and rawinsounding on October 17th 00:00–03:00 LT (a), and WALI derived parameters: extinction coefficient (α_a), VDR, WVMR (r_H) and LR for sampled times of Table 2, i.e. October 17th 00:00–03:00 LT (b), October 18th 00:00–03:00 LT (c), October 18th 10:30–14:30 LT (d), October 18th 21:00–00:00

LT (e), October 19th 00:00–03:00 LT (f), October 19th 03:00–06:00 LT (g), October 20th 00:00–03:00 LT (h). The time periods from a) to f) correspond to the ones of Table 2.

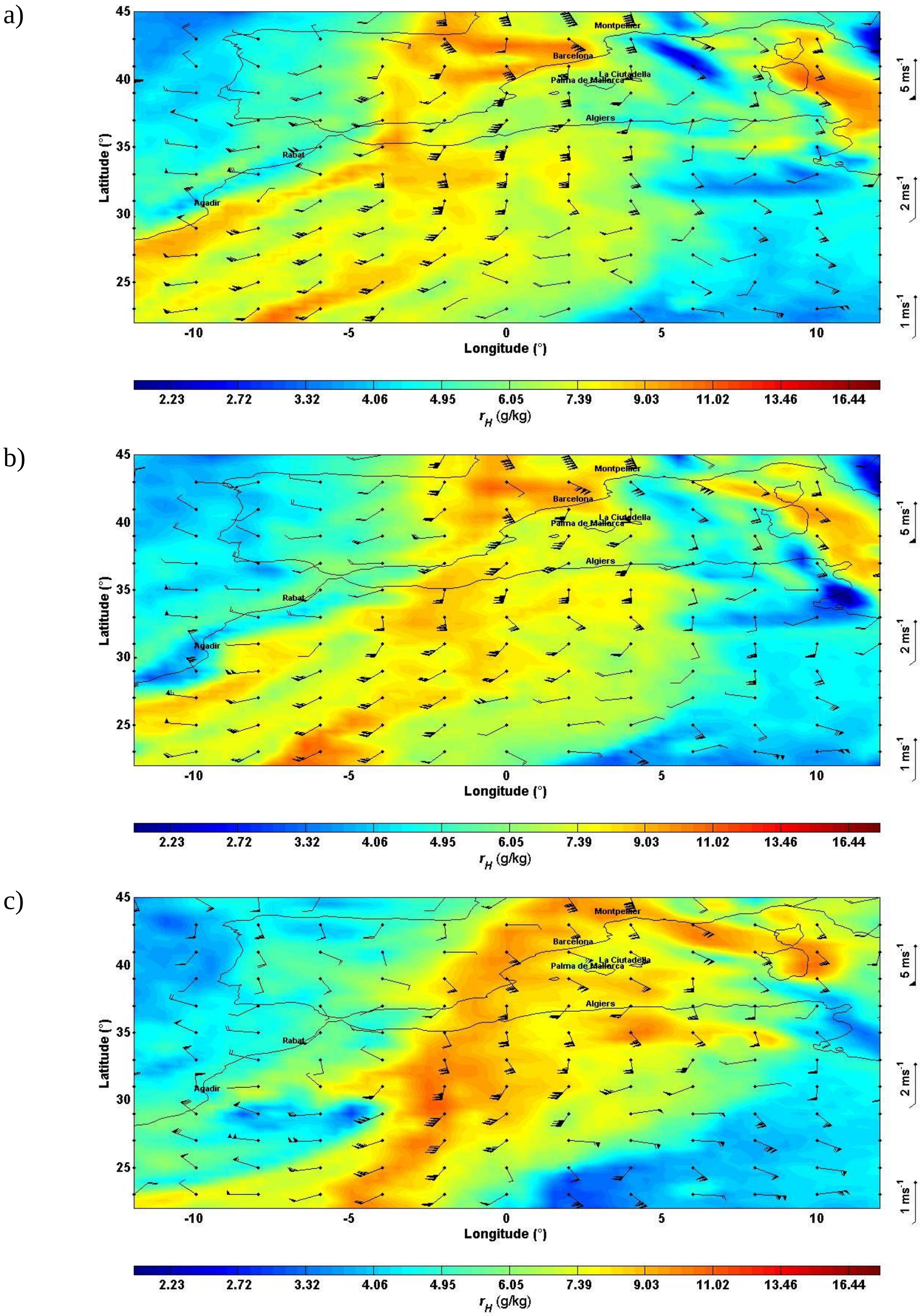

Figure 15: Wind-field (wind barbs) and WVMR (r_H) (color plot) from ECMWF OPERA 0.5° horizontal resolution analysis at 850 hPa level for October 19th at 02:00 LT (a), October 19th 08:00 LT (b), and October 20th 02:00 LT (c).